

1 **An automatic lake-model application using near real-time data**
2 **forcing: Development of an operational forecast workflow**
3 **(COASTLINES) for Lake Erie**

4 Shuqi Lin¹, Leon Boegman¹, Shiliang Shan², Ryan Mulligan¹

5 ¹Department of Civil Engineering, Queen's University, Kingston ON Canada K7L 3N6

6 ²Department of Physics and Space Science, Royal Military College of Canada, Kingston ON Canada K7K 7B4.

7 *Correspondence to:* Shuqi Lin (shuqi.lin@queensu.ca)

8 **Abstract.** For enhanced public safety and water resource management, a three-dimensional operational lake
9 hydrodynamic forecasting system COASTLINES (Canadian cOASTal and Lake forecastINg modEl System) was
10 developed. The modelling system is built upon the Aquatic Ecosystem Model (AEM3D) model, with predictive
11 simulation capabilities developed and tested for a large lake (i.e., Lake Erie). The open-access workflow derives
12 model forcing, code execution, post-processing, and web-based visualization of the model outputs, including water
13 level elevations and temperatures, in near real-time. COASTLINES also generates 240-h predictions using
14 atmospheric forcing from 15 km and 25 km horizontal-resolution operational meteorological products from the
15 Environment Canada Global Deterministic Forecast System (GDPS). Simulated water levels were validated against
16 observations from 6 gauge stations, with model error increasing with forecast horizon. Satellite images and lake
17 buoys were used to validate forecast lake surface temperature and the water column thermal stratification. The
18 forecast lake surface temperature is as accurate as hindcasts, with a root-mean-square-deviation <2°C.
19 COASTLINES predicted storm-surges and up-/down-welling events that are important for coastal flooding and
20 drinking water/fishery management, respectively. Model forecasts are available in real-time at
21 <https://coastlines.engineering.queensu.ca/>. This study provides an example of the successful development of an
22 operational forecasting workflow, entirely driven by open-access data, that may be easily adapted to simulate
23 aquatic systems or to drive other computational models, as required for management and public safety.

24 **1 Introduction**

25 Lakes hold a large proportion of the global surface freshwater, which supports biodiversity and supplies water
26 resources for drinking, transportation, and recreation. However, anthropogenic stressors are causing significant
27 changes in the properties of lakes, such as rapid warming of surface water (O'Reilly et al., 2015), large seasonal
28 water level fluctuations (Gronewold and Rood, 2019), increased frequency of extreme events (Saber et al., 2020)
29 and severe water quality issues such as oxygen depletion (Rowe et al., 2019; Scavia et al., 2014) harmful algal
30 blooms (Brookes and Carey, 2011; Watson et al., 2016). Effort has focussed on investigating the long-term
31 responses of physical processes in lakes to climate change (O'Reilly et al., 2015; Woolway and Merchant, 2019;
32 Jabbari et al., 2021), but improving lake monitoring and developing short-term forecast models, to predict the
33 occurrence of extreme events is also necessary (Woolway et al., 2020). The biogeochemical cycles in lakes are
34 complex and often regulated by physical forcing; therefore, the first step to model and forecast water quality issues,
35 such as harmful algal blooms (Paerl and Paul, 2012; O'Neil et al., 2012) and hypoxia (Rao et al., 2008; Rao et al.,
36 2014) is the development of accurate hydrodynamic models.

37 Over the past several decades, many computer models have been applied to hindcast (running models
38 forced with and validated against historically collected data) lake hydrodynamics to aid management. These range
39 from one-dimensional (1D) models such as DYRESM (Antenucci and Imerito, 2000), Simstrat (Gaudard et al.,
40 2017), and GLM (Hipsey et al., 2014), to three-dimensional (3D) models such as Delft3D (Lesser et al., 2004),
41 FVCOM (Chen et al., 2012; Rowe et al., 2019) ELCOM (Hodges et al., 2000). Several of these hydrodynamic
42 models may be coupled to biogeochemical models to allow for prediction of water quality. In the case of hindcast
43 applications, the complex and time-consuming setup and calibration procedure, of these models, can result in a
44 significant time lag (months to years) between when a project is initiated and when the model results are
45 communicated to stakeholders. This delay severely limits the utility of computational models for policy and
46 management decision making. For better application of these powerful computational tools, the ability for rapid
47 monitoring and simulation forecasts should be established.

48 In addition to the significant effort required to setup and calibrate models, other hurdles exist such as data-
49 sharing agreements between the agencies collecting forcing/validation data and those running the models. For
50 example, the US National Oceanic and Atmospheric Administration (NOAA) Great Lakes Coastal Forecasting
51 System (Chu et al., 2011; Anderson et al., 2018), is a comparatively large-budget multi-institutional (NOAA-
52 GLERL and U. Michigan-CIGLR) project that predicts water levels, temperature profiles, currents, and wave
53 heights over a 120-h timeframe in the five Laurentian Great Lakes and connecting channels, using FVCOM on a 3D
54 unstructured grid with 30-2000 m horizontal resolution. Similarly, meteolakes.ch (Baracchini et al., 2020b) applies
55 Delft3D for short-term 3D forecasts (4.5 days) of four Swiss lakes and simstrat.eawag.ch (Gaudard et al., 2019)
56 applies Simstrat for near-realtime 1D simulation of 54 Swiss lakes. These latter applications employ a data sharing
57 agreement between Swiss Federal Institute of Aquatic Science and Technology (EAWAG), École Polytechnique
58 Fédérale de Lausanne (EPFL) and MeteoSwiss.

59 Owing to the present online proliferation of near real-time lake observation data (e.g., National Data Buoy
60 Center (NDBC; <https://www.ndbc.noaa.gov/>); Great Lakes Observation System (GLOS; <https://www.glos.us/>) and

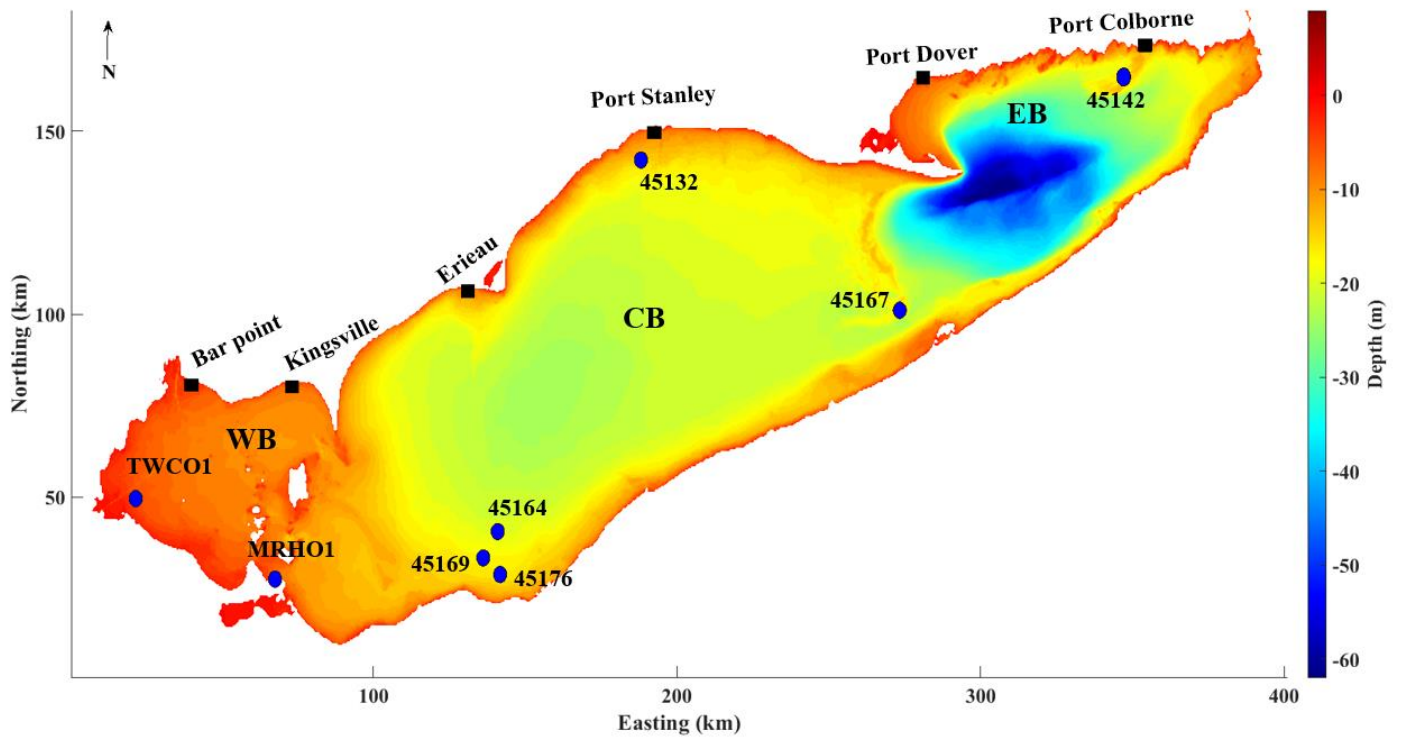
61 high-resolution meteorological forecasts (e.g., Global Deterministic Prediction System, GDPS;
62 https://dd.weather.gc.ca/model_gem_global/; High Resolution Rapid Refresh, HRRR;
63 <https://rapidrefresh.noaa.gov/hrrr/>) the data-sharing agreements and managed data transfer protocols are no longer
64 required. When coupled with recent dramatic improvements in workflow efficiency (e.g., Gaudard et al. (2019);
65 Baracchini et al. (2020b)) near real-time inclusion of forcing from meteorological forecasts allow for the
66 development of specific simulations tailored to meet diverse lake-management needs (e.g., prediction of coastal
67 flooding, spill modelling, fish habitat, beach closures, and optimization of treatment or source water monitoring
68 strategies).

69 In the present study we developed and tested the COASTLINES (Canadian cOASTal and Lake forecastINg
70 modEl System; <https://coastlines.engineering.queensu.ca/>) lake-model application workflow, that rapidly accesses
71 near real-time online data (weather forecasts, water level and temperature observations) for automated model
72 forcing, execution and validation. Hydrodynamic forecasts are automatically post-processed and posted on a web
73 platform. We provide an overview of the COASTLINES system, including model implementation for Lake Erie
74 (Section 2 Data and methods) and the accuracy of COASTLINES in forecasting water levels and temperature fields
75 over timescales of 24-h and 240-h (Section 3 Results). In Section 4 Discussion, the predictive ability of
76 COASTLINES for decision making is showcased through prediction of hydrodynamic events associated with fish
77 kills, hypoxia near a drinking water intake and coastal flooding from a storm surge. We also discuss the relative
78 advantages of COASTLINES in comparison to other model products, including bias and uncertainty.

79 **2 Data and methods**

80 **2.1 Study site**

81 Lake Erie, the shallowest lake of the Great Lakes with a mean depth of 19 m. Lake-wide hydrodynamics
82 predominantly exhibits free surface and current oscillations from the 14-h barotropic seiche (Hamblin, 1987;
83 Boegman et al., 2001). The lake morphometry consists of distinct, yet interconnected western, central, and eastern
84 basins (Fig. 1), each with its own water quality concerns: The 11-m deep western basin is typically well mixed and
85 has frequent harmful algae blooms related to climate-driven meteorological forcing (Michalak et al., 2013). The
86 ephemeral stratification in late summer (Loewen et al., 2007) regulates vertical biogeochemical fluxes (Boegman et
87 al., 2008). The 20-m deep central basin is prone to large-scale hypolimnetic hypoxia (Scavia et al., 2014).
88 Hydrodynamics are governed by an internal Poincaré wave (Bouffard et al., 2012; Valipour et al., 2015) and a bowl-
89 shaped depression of the summer thermocline, which influence the oxygen budget (Beletsky et al., 2012; Bouffard et
90 al., 2014). The 65-m deep eastern basin has nearshore water quality concerns from *cladophora* (Higgins et al., 2006)
91 and ecosystem engineering by dreissenid mussels (Hecky et al., 2004). Hydrodynamics of this region are controlled
92 by the coastal internal Kelvin wave (Valipour et al., 2019).



94 **Fig.1** Map of Lake Erie showing the bathymetric depths and observation sites. The bathymetric map is at the
 95 resolution of the 500 m grid applied in the model. The western, central, and eastern basins are labeled as WB,
 96 CB, and EB, respectively. Blue circles indicate lake buoys and black squares indicate water level gauges.

97 **2.2 Model description**

98 COASTLINES applies the three-dimensional Aquatic Ecosystem Model (AEM3D, version 1.1.1, HydroNumerics
 99 Pty Ltd.). This model solves the unsteady 3D Reynolds-averaged Navier-Stokes equations for incompressible flow
 100 employing the Boussinesq and hydrostatic approximations. Momentum advection is based on the Euler-Lagrange
 101 method with a conjugate-gradient solution for the free-surface height (Casulli and Cheng, 1992), and a conservative
 102 ULTIMATE QUICKEST discretization scheme for advection of scalars (Leonard, 1991). AEM3D is a parallel
 103 version of the commonly applied Estuary and Lake Computer Model (ELCOM; (Hodges et al., 2000). ELCOM has
 104 been applied to Lake Erie to simulate currents and seasonal circulation (León et al., 2005), the internal Poincaré
 105 (Valipour et al., 2015) and Kelvin waves (Valipour et al., 2019), ice cover (Oveisly et al., 2012) and the response of
 106 the thermal structure, in Lake Erie, to air temperature and wind speed changes (Liu et al., 2014). ELCOM has been
 107 coupled with the biogeochemical CAEDYM model to simulate Lake Erie phytoplankton and nutrients (León et al.,
 108 2011), and the response of hypoxia (Bocaniov and Scavia, 2016) and algae blooms (Scavia et al., 2016) to nutrient
 109 load reductions. Recent applications of AEM3D include a study of the water level in Lake Arrowhead, California
 110 (Saber et al., 2020), ice cover in Lake Constance (Caramatti et al., 2019) and pollutant transport in Lake St. Clair
 111 (Madani et al., 2020).

112 **2.3 Model setup and meteorological forcing variables**

113 To adequately resolve the coastal boundary layer (~ 3 km width (Rao and Murthy, 2001)) and basin-scale internal
114 waves (Poincaré (16.8 h) and Kelvin waves), the bathymetry of Lake Erie
115 (<https://www.ngdc.noaa.gov/mgg/greatlakes/erie.html>) was discretized into a 500 m × 500 m horizontal grid, which
116 is ~10 % of the internal Rossby radius (Schwab and Beletsky, 1998). The lake was discretized into 45 vertical
117 layers, with fine resolution (0.5 m) through the surface layer, metalimnion and bottom of the central basin, and
118 coarse layers (5 m) through the hypolimnion of the deeper eastern basin to the maximum depth of 64 m.
119 The model was ‘cold started’ on April 8, 2020 (day of year (day) 99) with an initial temperature field spatially
120 interpolated from observed water temperatures at stations 45142 and MHRO1; a time when spring turnover causes
121 thermal stratification to be minimal. The model time step is $dt = 300$ s to satisfy the $CFL = \sqrt{2}$ (Courant-Friedrichs-
122 Lewy) condition for internal waves (Hodges et al., 2000).

123 The model is forced by the surface meteorology (wind speed, wind direction, air temperature, shortwave
124 solar radiation, relative humidity, air pressure, and net longwave radiation), with net longwave radiation being
125 computed internally within AEM3D from cloud cover and the modelled surface temperature. In order to address the
126 spatial variability of meteorological conditions across the lake, the computational domain was forced with
127 meteorological data on horizontal grids at 15 km (https://dd.weather.gc.ca/model_gem_global/15km/) and 25 km
128 (https://dd.weather.gc.ca/model_gem_global/25km/) resolution using meteorological forecasts from the
129 Environment and Climate Change Canada Global Deterministic Forecast System (GDPS). This resulted in 31 and 23
130 meteorological sections for the 15 km and 25 km models, respectively. Wind speed, wind direction, air temperature,
131 relative humidity, air pressure, dew point, and cloud cover are direct outputs from GDPS, with solar radiation
132 calculated based on dew point and air pressure ((Meyers and Dale, 1983); Appendix C. in (Gaudard et al., 2019)).
133 The meteorological forecast has an output timestep of 3-h and a forecast length of 240 h. The .GRIB2
134 meteorological data were retrieved with the ‘urllib’ library in Python and formatted into AEM3D input files using
135 the nctoolbox in MATLAB.

136 In this pilot application, the Lake Erie inflows and outflows, which roughly balance, are neglected,
137 however evaporation and precipitation are accounted for in the water balance. Over short timescales (<10 days), the
138 contributions from evaporation and precipitation to water level change are minor, with water level oscillations
139 resulting from storm surges and surface seiches (Trebitz, 2006).

140 **2.4 Observations, implementation, and model validation**

141 The water levels and temperatures simulated by COASTLINES were validated using both in situ and satellite
142 observations. Near real-time water level data was used from six stations along the Canadian coastline, which
143 reported hourly observations (Bar Point, Kingsville, Erieau, Port Stanley, Port Dover, and Port Colborne; Fig. 1;
144 Table 1), retrieved from Fisheries and Oceans Canada (<https://marees.gc.ca/eng/find/zone/44>). The data are parsed
145 using the ‘BeautifulSoup’ library in Python and saved as .csv files, to be read with MATLAB for model validation.
146 The observations showed higher fluctuations in the western (Bar Point and Kingsville) and eastern (Port Dover and

147 Port Colborne) basins (Fig. 1). Thus, we quantify the water level forecast capability and uncertainty in terms of the
148 Root Mean Square Deviation (RMSD) and Relative Error (RE):

$$149 RMSD = [\frac{1}{N} \sum_{i=1}^N (x_i - y_i)^2]^{1/2}, \quad (1)$$

$$150 RE = 100 \frac{RMSD}{\log. \text{mean}(\text{daily range})}, \quad (2)$$

151 where x_i and y_i ($i = 1, 2, 3, \dots N$) are the model and observed water level timeseries and N is the number of samples.
152 RMSD is the absolute error of the model against the observation. The difference between the observed daily
153 minimum and maximum value was defined as the daily water level fluctuation range, where RE is the ratio between
154 the RMSD and lognormal mean of daily range over April to September 2020. Given that our study focusses on a
155 240-h forecast, RE is able to characterize the forecast bias, regardless of the instantaneous water level position.

156 Eight in situ lake buoys, distributed over the nearshore areas of the three basins (Fig. 1; Table 1), provided
157 near real-time model validation data through the Great Lakes Observing System (GLOS: <https://www.glos.us/>) and
158 National Data Buoy Center (NDBC: <https://www.ndbc.noaa.gov/>) portals. For each station, the text-based NDBC
159 observations are parsed using the ‘BeautifulSoup’ Python library, and the GLOS observations are retrieved using
160 ‘webdriver’ from the ‘selenium’ Python library. All the lake buoy observations are saved as .csv files and read into
161 MATLAB for post-processing. Attempts to retrieve missing variables would result in run-time errors.

162 The lake buoys are deployed from April or May through mid-October, spanning the spring/fall turnover
163 and seasonal summer stratification periods. However, due to COVID-19 related delays in instrument deployments in
164 2020, only two buoys located offshore of Cleveland, near the water intake crib (station 45176 and station 45164),
165 were equipped with thermistor chains to monitor temperature profiles. The other six buoys provide air and lake
166 surface temperature as well as wind speed and direction observations for hydrodynamic and meteorological forecast
167 validation. Satellite-based observations of lake surface temperature were obtained from the Great Lakes Surface
168 Environmental Analysis (GLSEA2), which is derived from NOAA CoastWatch AVHRR (Advanced Very High-
169 Resolution Radiometer) imagery and updated on NOAA GLERL website
[\(https://coastwatch.glerl.noaa.gov/erddap/files/GLSEA_GCS/\)](https://coastwatch.glerl.noaa.gov/erddap/files/GLSEA_GCS/). GLSEA2 produced daily observations, with 2.6 km
170 resolution, from the cloud-free portions of the satellite images (Schwab et al., 1999). The netCDF data are retrieved
171 using the ‘BeautifulSoup’ library and ‘webdriver’ from ‘selenium’.
172

173 We quantified the temperature forecast capability using the statistical measures of RMSD (eq. 1) and Mean
174 Bias Deviation (MBD):

$$175 MBD = 100 \frac{\frac{1}{N} \sum_{i=1}^N (x_i - y_i)}{\frac{1}{N} \sum_{i=1}^N y_i} \quad (3)$$

176 For the spatial MBD and RMSD (s-MBD and s-RMSD), x_i and y_i are the model and observed temperature in each
177 grid, and N is the total number of grids. For timeseries MBD and RMSD (t-MBD and t-RMSD), x_i and y_i are the
178 model and observed temperature at each sample time, and N is the total number of samples.
179
180

181 **Table 1**
 182 **Details of field stations with water level gauges and lake buoys.**

Station	Parameter	Sampling interval (min)	Depth of measurement (m)
Bar Point	Water level	60	Surface
Kingsville	Water level	60	Surface
Erieau	Water level	60	Surface
Port Stanley	Water level	60	Surface
Port Dover	Water level	60	Surface
Port Colborne	Water level	60	Surface
TWCO1	Temperature	10	Surface
45005	Temperature	10	Surface
45176	Temperature	10	1, 3, 4, 6, 7, 9, 10, 12, 14, 15
45169	Temperature	30	surface
45164	Temperature	60	1, 2, 4, 6, 8 10
45132	Temperature	60	Surface
45167	Temperature	10	Surface
45142	Temperature	60	Surface

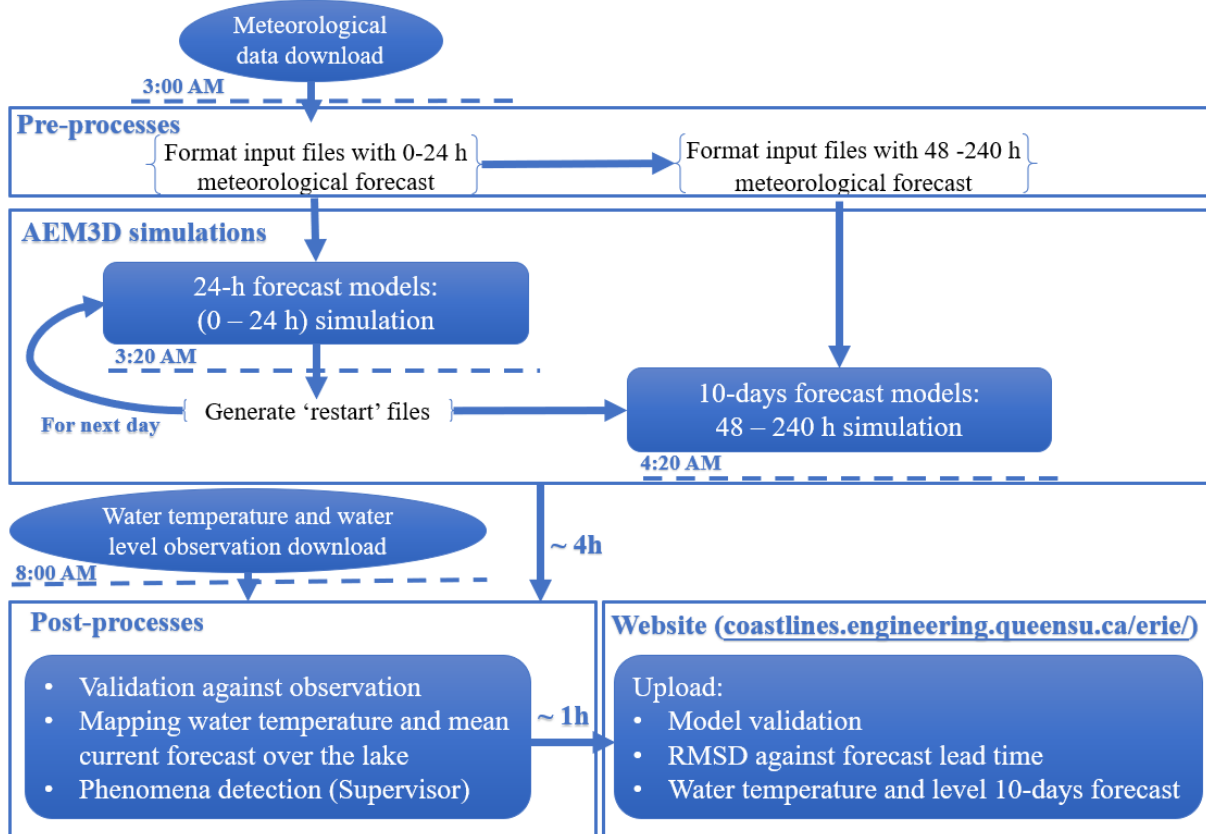
183 **2.5 System operation**

184 The COASTLINES operational forecast system is run on a local server supported by Queen's University ITS
 185 (Kingston, Canada). The COASTLINES workflow is presented in Fig. 2. The system consists of input data
 186 acquisition and preparation, 24-h hydrodynamic simulations, 240-h hydrodynamic simulations, validation against in
 187 situ observations, and uploading the model forecasts and validation to the web platform. Given that the standard
 188 deviations of meteorological forecast variables increase with forecast lead time (Buehner et al., 2015), we performed
 189 separate 24-h and 240-h forecast simulations each day. The model advances every day according to the 24-h forecast
 190 simulation and terminates by generating 're-start' files. These files are then used to hot-start the 240-h forecast
 191 simulation and the 24-h simulations for the next day. The input files for the 240-h forecast simulations are
 192 iteratively replaced by the new 240-h meteorological forecast generated each day. The 24-h and 240-h forecast
 193 model outputs are compared against observations to evaluate the forecast performance against forecast lead time.

194 The long-term stability of employing daily 'hot' restarts can be seen in a comparison between simulated
 195 temperature profiles from a continuous run and that from stitching together the 24-h hot-start simulations (Appendix
 196 A; Fig. A1). At present, the initial water level cannot be modified using the AEM3D re-start files. Therefore, to
 197 account for long term drift in surface water level, we used real time gauge observations as the datum point for water
 198 level forecasts (automatically performed by MATLAB in post processing) and only consider errors resulting from
 199 simulation of storm surges and seiches, as opposed to those from seasonal changes in mean lake level. Automation
 200 of the processing tasks in the workflow is performed by Python scripts triggered by the Windows Task Scheduler
 201 every 24-h at midnight. The online meteorological forecast data are retrieved from GDPS once updated at 3 am
 202 EST. Forcing variables are then formatted in MATLAB, called by the Python scripts once the meteorological
 203 forecast data has been retrieved. The AEM3D pre-compiled executable is then run as a black-box code, triggered by
 204 Python. The 24-h and 240-h simulations take 0.5 h and 4 h to complete, respectively. The observed data, including
 205 water levels from gauge stations, water temperatures from lake buoys and satellite images are scraped with Python
 206 at 8 am, followed by post-processing in MATLAB to validate model output, calculate statistical metrics (RMSD,
 207 MBD) and generate figures. The results are exported to Google sheets and published to the COASTLINES website

208 (e.g., Appendix B). The authors (supervisors of COASTLINES) and Queen's ITS monitor forecast results and
209 maintain system operation.

210 Global coverage of the GDPS forecasts enable this operational system to be readily implemented at other
211 sites where lake bathymetry, boundary flows and in-situ validation data are available. The workflow may be easily
212 modified to include additional meteorological forecasts or black-box hydrodynamic drivers (e.g., HRRR and
213 Delft3D, respectively (Rey and Mulligan, 2021)).



214

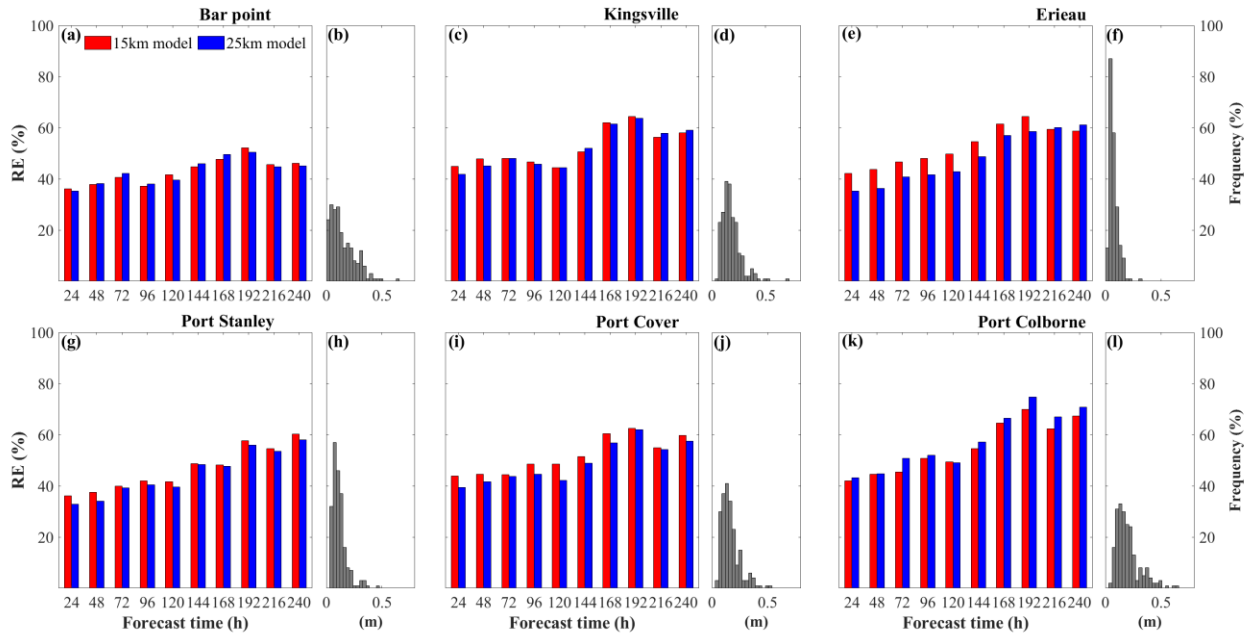
215 **Fig. 2 Daily workflow and automated processes in the COASTLINES operational system as performed on the**
216 **local server.**

217 3 Results

218 The COASTLINES water level and temperature forecasts have been operational since April and July 2020,
219 respectively. The 24-h and 240-h forecast water levels from the 15 km and 25 km resolution models were validated
220 against real-time gauge station observations. The water level statistical metrics (RMSD and RE) were ensembled
221 and averaged over April to September 2020. The 24-h and the 240-h forecast lake surface temperature and
222 temperature profiles, from the models, were also validated against real-time lake buoy data and daily averaged
223 satellite imagery. The timeseries and spatial MBD and RMSD (t-RMSD, t-MBD and s-RMSD, s-MBD) were
224 ensembled and averaged over July to September 2020.

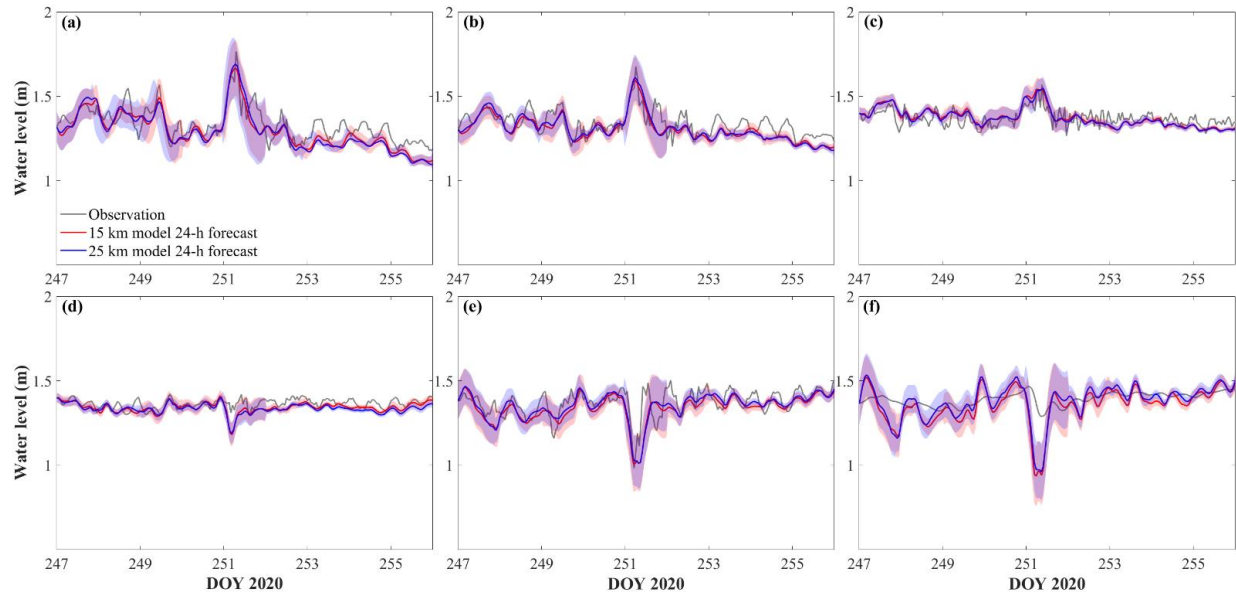
225 **3.1 Water level**

226 The Relative Error (RE) of the forecast water level increases with forecast time when averaged over April to
 227 September 2020; the 24-h forecast error being ~ 40% at all six gauge stations (Fig. 3 a, c, e, g, i, k). Given the large
 228 water level fluctuation at Port Colborne (Fig. 3 l), the 240-h forecast RE is highest at this station, exceeding 70%
 229 (Fig. 3 k). Of the six gauge stations reported in this study, those at the western (Bar Point and Kingsville) and
 230 eastern (Port Dover and Port Colborne) ends of Lake Erie longitudinal axis had the largest water level fluctuations,
 231 resulting from the predominant south-westerly winds generating strong wind set-up and surface seiches (Fig. 3 b, d,
 232 f, h, j, l). The lognormal means of the daily range in water level at the six gauge stations are 0.21 cm (Bar Point),
 233 0.16 cm (Kingsville), 0.07 cm (Erieau), 0.10 cm (Port Stanley), 0.15 cm (Port Dover), 0.17 cm (Port Colborne).
 234 The 24-h forecasts show qualitative agreement with observations in phase and magnitude (Fig. 4). The 24-h
 235 forecasts reproduce the dramatic surface seiches induced by westerly winds $> 15 \text{ m s}^{-1}$ (Fig. C2) on day 251 (RMSD
 236 $< 0.1 \text{ cm}$), especially the obvious water level fluctuations at stations in the western and eastern basins (Fig. 4 a, b, e).
 237 However, the prediction of water level at Bar Point showed large bias (Fig. 4 f), with the model overestimating the
 238 water level fluctuation. The uncertainty in the model forecast, which increased with the range of the daily
 239 fluctuation, was captured by the ensemble 24-h forecast RE over April to September (the shaded areas in Fig. 4).
 240 Overall, the confidence interval of the 24-h forecast included most of the discrepancies between the observations
 241 and the model results.



242

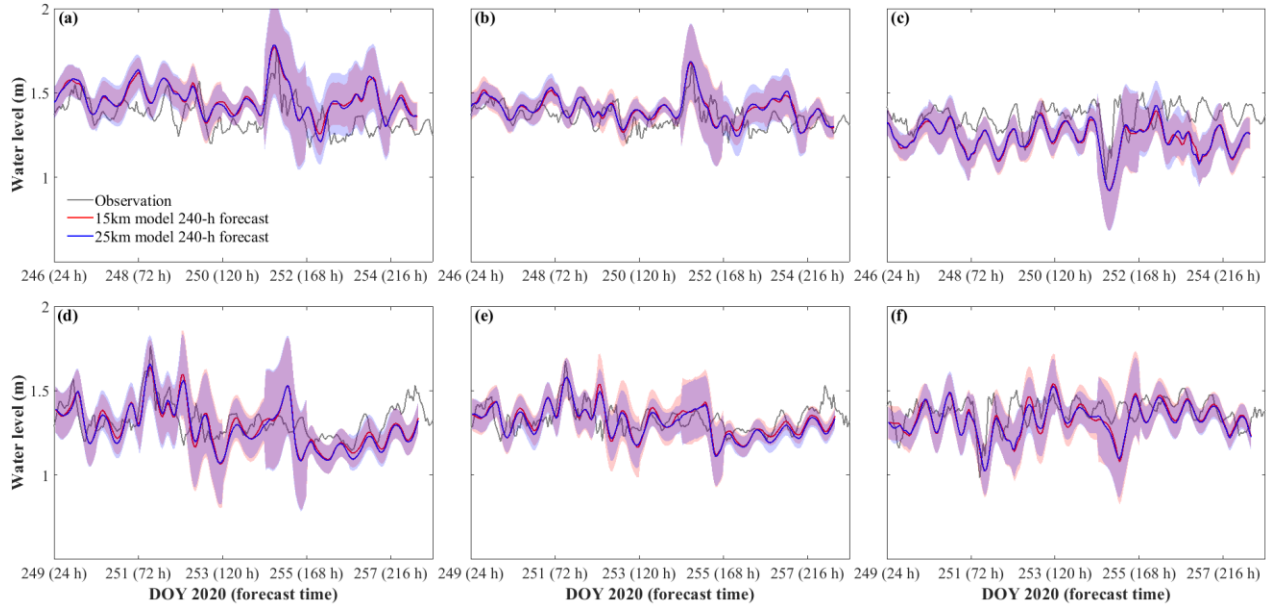
243 **Fig. 3 Relative error (RE) in water level predictions against forecast time at six stations (a, c, e, g, i, k).** Panels
 244 **Fig. 3 Relative error (RE) in water level predictions against forecast time at six stations (a, c, e, g, i, k).** Panels
 245 **Fig. 3 Relative error (RE) in water level predictions against forecast time at six stations (a, c, e, g, i, k).** Panels
 246 **Fig. 3 Relative error (RE) in water level predictions against forecast time at six stations (a, c, e, g, i, k).** Panels



247

248 **Fig. 4 Comparison between observed and stitched 24-h forecast modeled water level at (a) Port Colborne, (b)**
 249 **Port Dover, (c) Port Stanley, (d) Erieau, (e) Kingsville, and (f) Bar Point. The shaded areas show the confidence**
 250 **interval of the 15 km model (red shading) and the 25 km model (blue shading), as given by the ensemble 24-h**
 251 **RE in Fig. 3.**

252 Timeseries validations for the 240-h model forecast (Fig. 5) include confidence intervals from the ensemble RE
 253 (Fig. 3). As shown, the forecast began 6 days in advance of the large surface seiche event on day 251 and predicted
 254 the seiche to crest at Port Colborne 1-2 h ahead of the observations, and to trough at Kingsville 1-2 h behind the
 255 observations (Fig. 5 a, c). Damping of the seiche oscillations (~144 hours in the future) was excessive, with the
 256 water levels being underestimated and the phase shifted by approximately 12 hours (Fig 5. a, b). Despite the wide
 257 confidence intervals, due to the increasing RE with forecast time, large bias existed after the seiche event (forecast
 258 time >168 hours). When the forecast was initiated close to the event (3 days before), the prediction of seiche phase
 259 was more accurate (Fig. 5 d, e, f); however, the seiche decay still had a 12-h phase shift. The discrepancies in seiche
 260 amplitude (< 0.1 m) were within the confidence intervals of the models.



261

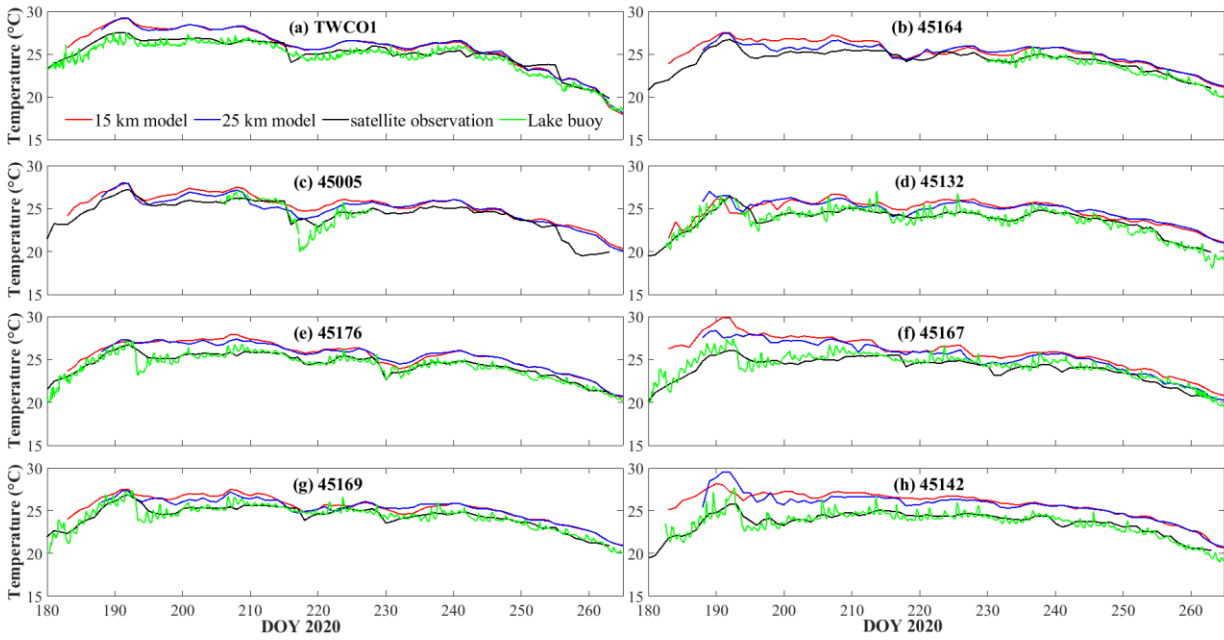
262 **Fig. 5 Comparison between the observed water level and 240-h forecast hot-started on day 245 (a, b, c) and day**
 263 **248 (d, e, f) at Port Colborne, Port Dover, and Kingsville, respectively. The shaded areas show the confidence**
 264 **interval of the 15 km model (red shading) and the 25 km model (blue shading), as given by the ensemble 240-h**
 265 **RE in Fig. 4.**

266 **3.2 Water temperature**

267 **3.2.1 Lake surface temperature**

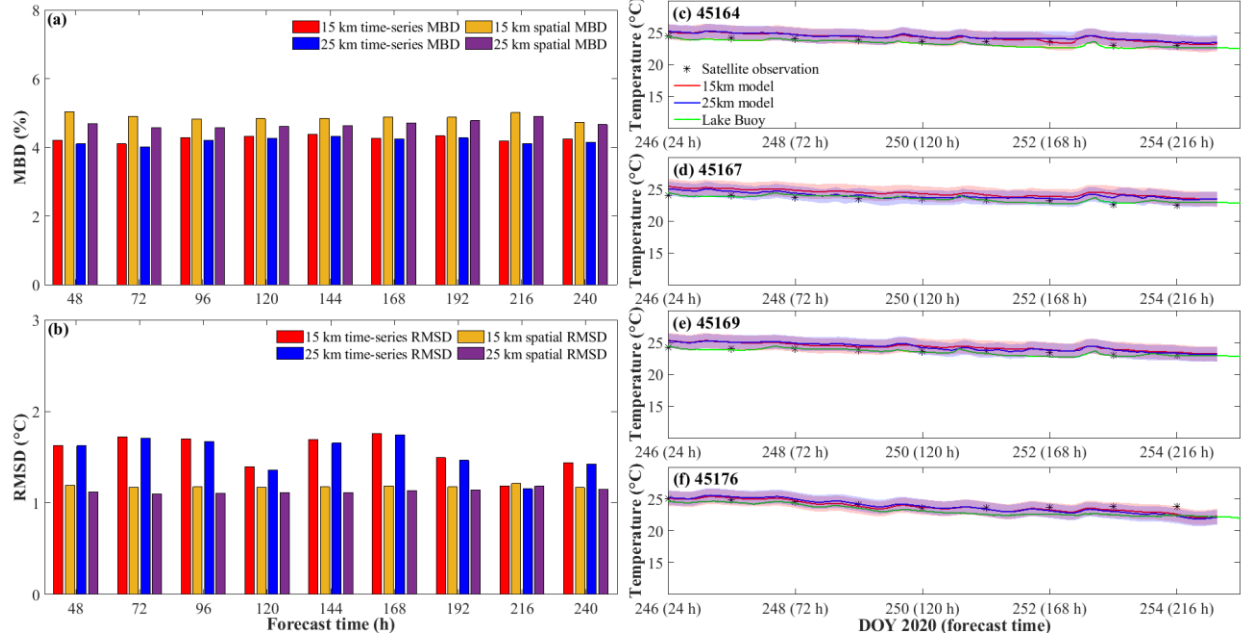
268 Using satellite-based and lake buoy-based observations, we evaluated the lake surface temperature forecast (Fig. 6).
 269 The 24-forecast captured the seasonal variation of lake surface temperature, particularly the rapid increase in
 270 temperature on days 180-190, and the gradual decrease in temperature after day 240; at all eight stations. However,
 271 the forecast overestimated the lake surface temperature in July by 3-5 °C (days 180-210), particularly at STN 45167
 272 and 45142. Due to the 3-h output interval associated with the meteorological forecast data, the forecast model was
 273 insensitive to temperature fluctuations over shorter timescales, as recorded by the lake buoys, and it underestimated
 274 the sudden decrease in temperature near day 220 and 255 at STN 45005.

275 Overall, the t-MBD and t-RMSD, over these eight stations, were ~6% and 1.4 °C (15 km model) and ~5%
 276 1.3 °C (25 km model) for the 24-h forecast, respectively (Table 2). The average s-MBD and s-RMSD over the 50
 277 days from July-September were ~4% and 1.2 °C, respectively, for both 15 km and 25 km resolution models.



278

279 **Fig. 6 Comparison between the stitched 24-h forecast and observed lake surface temperature at 8 stations (a)**
 280 **(b) 45164, (c) 45005, (d) 45132, (e) 45176, (f) 45167, (g) 45169, and (h) 45142.** The green lines are
 281 timeseries observations from lake buoys, the black lines are daily observations derived from satellite imagery.



282

283 **Fig. 7 (a) Mean-Bias Deviation (MBD) against forecast time; (b) Root-Mean-Square Deviation (RMSD) against**
 284 **forecast time. (c-f) Timeseries of 240-h forecast and observed lake surface temperature at stations 45164, 45167,**
 285 **45169, 45176, respectively, and daily averaged satellite lake surface temperature (black asterisks).** The
 286 **confidence interval (shaded areas) in (c-f) represents the uncertainty of the 240-h forecast model through the**
 287 **timeseries RMSD with the forecast time (panel b).**

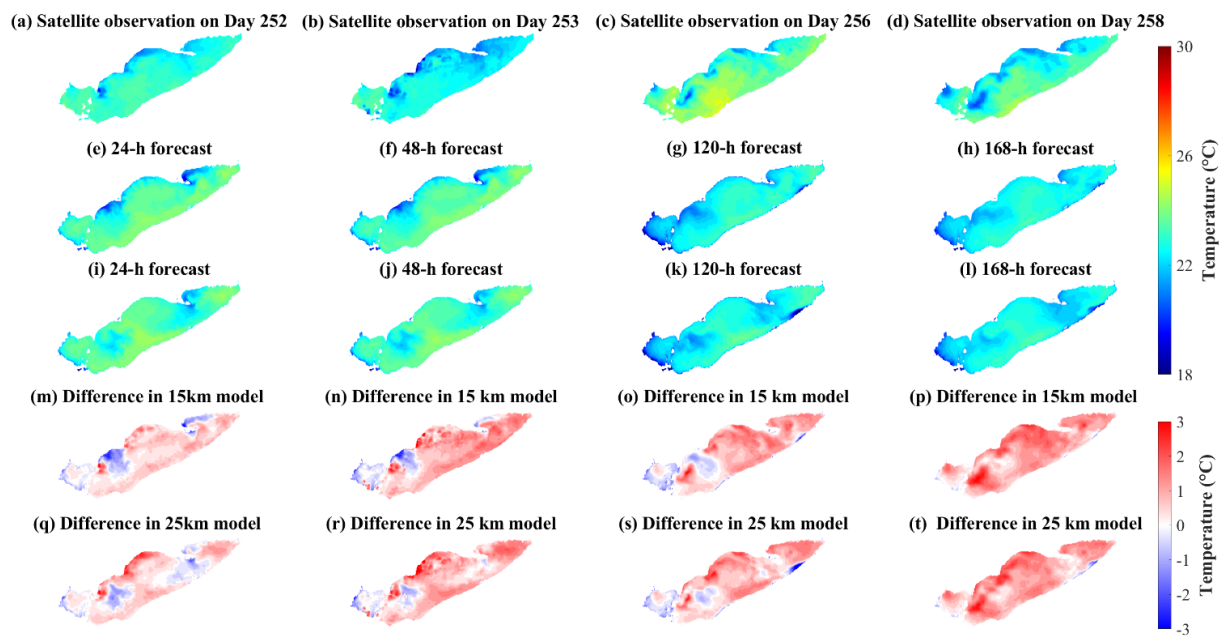
288 The 240-h forecast MBD and RMSD, surprisingly, do not show an increase in error with forecast time (Fig. 7 a, b).

289 Both t-MBD and s-MBD, over the 240-h forecast, are ~4-5%, with s-MBD 0.5-1% higher than t-MBD. Although

290 both 240-h s- and t-RMSD are under 2 °C, the t-RMSD show the error with forecast time to be higher than s-RMSD.
 291 Both timeseries observations from lake buoys and daily averaged observations from satellite imagery fall into the
 292 forecast confidence interval based on the 240-h t-RMSD (Fig 7 c-f).

293 Spatial comparisons of satellite-based observations to the 24-h, 48-h, 120-h, 168-h surface temperature
 294 forecasts illustrate that the forecast system (with 15 km meteorological data) predicted the cooler water mass along
 295 the northwest shoreline of the central basin with a cold bias ~ 2 °C (Fig. 8); this may be up-welling hypolimnetic
 296 water (see following Discussion 4.2). The model also predicted lower surface temperatures in coastal regions of the
 297 western basin with a cold bias ~2 °C (Fig. 8 m-t); the bias presumably was induced by neglecting riverine inflows
 298 (e.g., Detroit River and Maumee River; see also Discussion 4.3), which are typically near the air temperature and
 299 several degrees warmer than the lake surface (Wang and Boegman, 2021). Further comparisons between model
 300 predictions and satellite-based observations of lake surface temperature can be found in the Supporting material
 301 (Fig. D1-2).

302



303

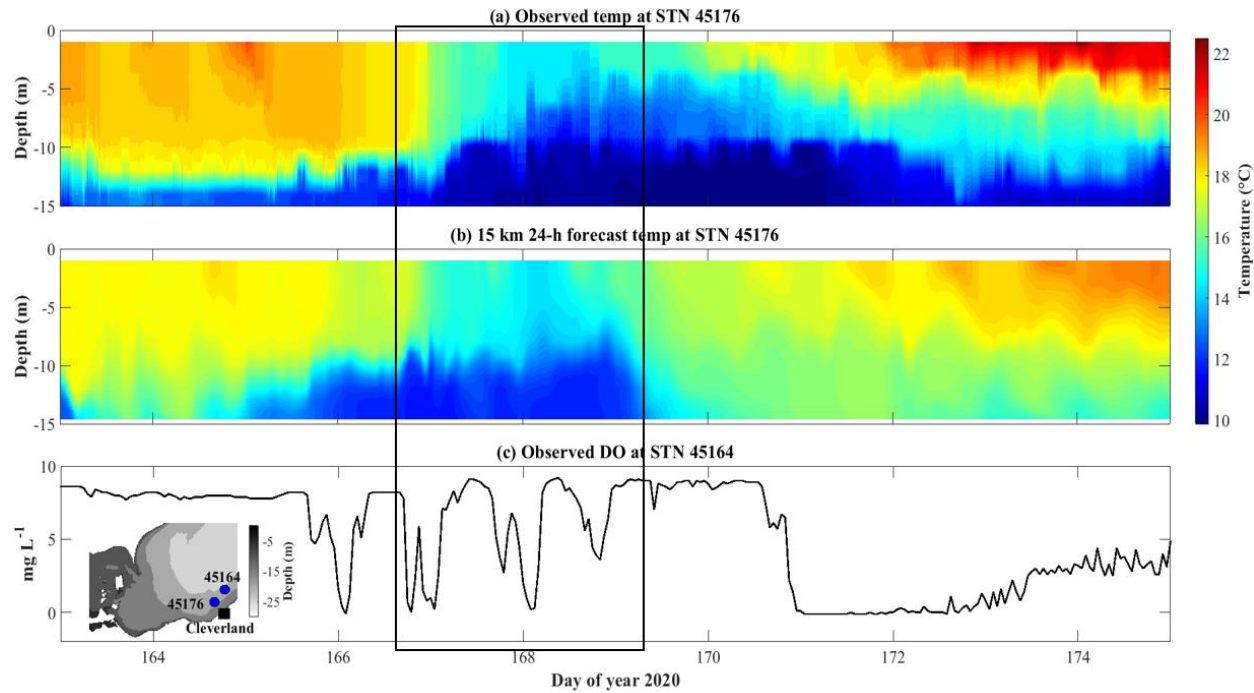
304 **Fig. 8 Comparison of lake surface temperature from (a-d) satellite observations, (e-h) 15 km model forecast,**
 305 **and (i-l) 25 km model forecast during late summer. The models were hot-started on day 251. The difference**
 306 **between observations and models are shown in (m-t).**

307 3.2.2 Thermal structure

308 The 3D AEM3D model structure applied in COASTLINES enables the prediction of the thermal profiles in the lake.
 309 On 15 Jun. 2020 (day 168), a rapid drop (~ 6°C) in surface temperature, was recorded by the thermistor at STN 45176,
 310 and predicted by the stitched 24-h COASTLINES model (15 km meteorological input) (Fig. 9 a, b). The timing and
 311 intensity of this up-welling event were accurately forecast, but before and after the upwelling event, the mixed layer
 312 depth was modelled to be deeper than observed; perhaps a result of spurious numerical diffusion resulting from the

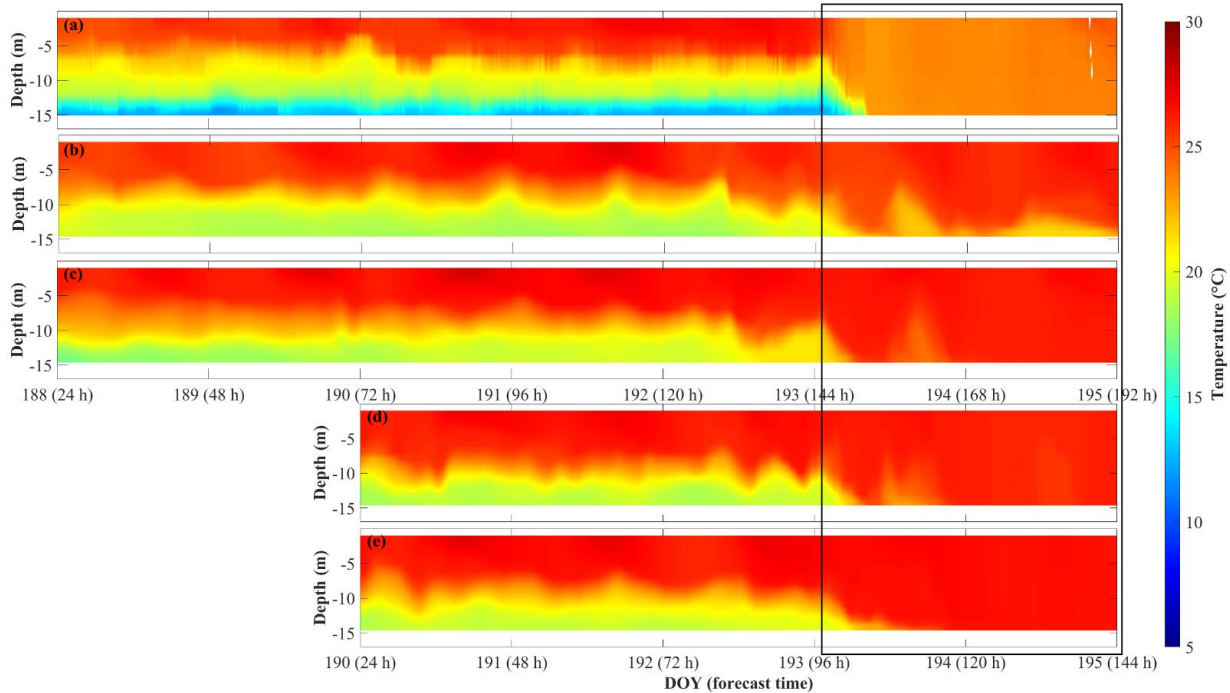
313 thermocline swashing along the stair-step z-level grid at the lake perimeter. The 240-h forecast model was not yet
314 operational at this time.

315 Both the 240-h 15 km and 25 km resolution forecasts predicted the down-welling event on 11 Jul. 2020 (day
316 193) at STN 45176 (Fig. 10). The forecasts were hot-started 7 days before the event (day 187), successfully predicting
317 when warm surface water down-welled toward the bed displacing the thermocline (Fig. 10 b, c), but the 15 km
318 resolution underestimated the intensity of down-welling, predicting thermocline recovery on day 193. The forecast
319 hot-started 5 days before the event (day 189) gave a more accurate prediction with the down-welling persisting over
320 2 days (Fig. 10 d, e) – as observed (Fig. 10 a).



321

322 **Fig. 9** Temperature profile comparisons between (a) observations and (b) stitched daily 24-h forecasts from the
323 15 km resolution model at station 45176. (c) Observed dissolved oxygen concentration at station 45164 from
324 lake buoy (<https://www.glos.us/>). The inset image shows the bathymetry and locations of lake buoys. The black
325 square indicates the timing of the up-welling event.



326

327 **Fig. 10 Comparisons of (a) observed temperature profile, (b, d) 240-h 15 km resolution modeled,**
 328 **and (c, e) 240-h 25 km resolution modeled temperature profiles at STN 45176.** The forecast models were hot-started on day
 329 **187 (b, c), and day 189 (d, e).** The black square indicates the down-welling event.

330 **Table 2**
 331 **Statistical measures of t-MBD (Mean-Bias Deviation) and t-RMSD (Root-Mean-Square Deviation) between**
 332 **the 24-h forecast model and observations of water temperature.**

Station	RMSD (°C)		MBD (%)	
	15 km model	25 km model	15 km model	25 km model
45176	2.6	2.6	6.8	6.8
45164	1.8	2.1	2.2	2.3
45132	1.5	1.5	5.5	5.7
45142	2.4	2.1	9.9	8.8
45167	1.2	1.1	4.6	4.0
45169	1.3	1.2	4.7	4.6
TWCO1	1.0	1.0	3	1.9
45005	1.2	1.1	8.2	7.9

333 4 Discussion

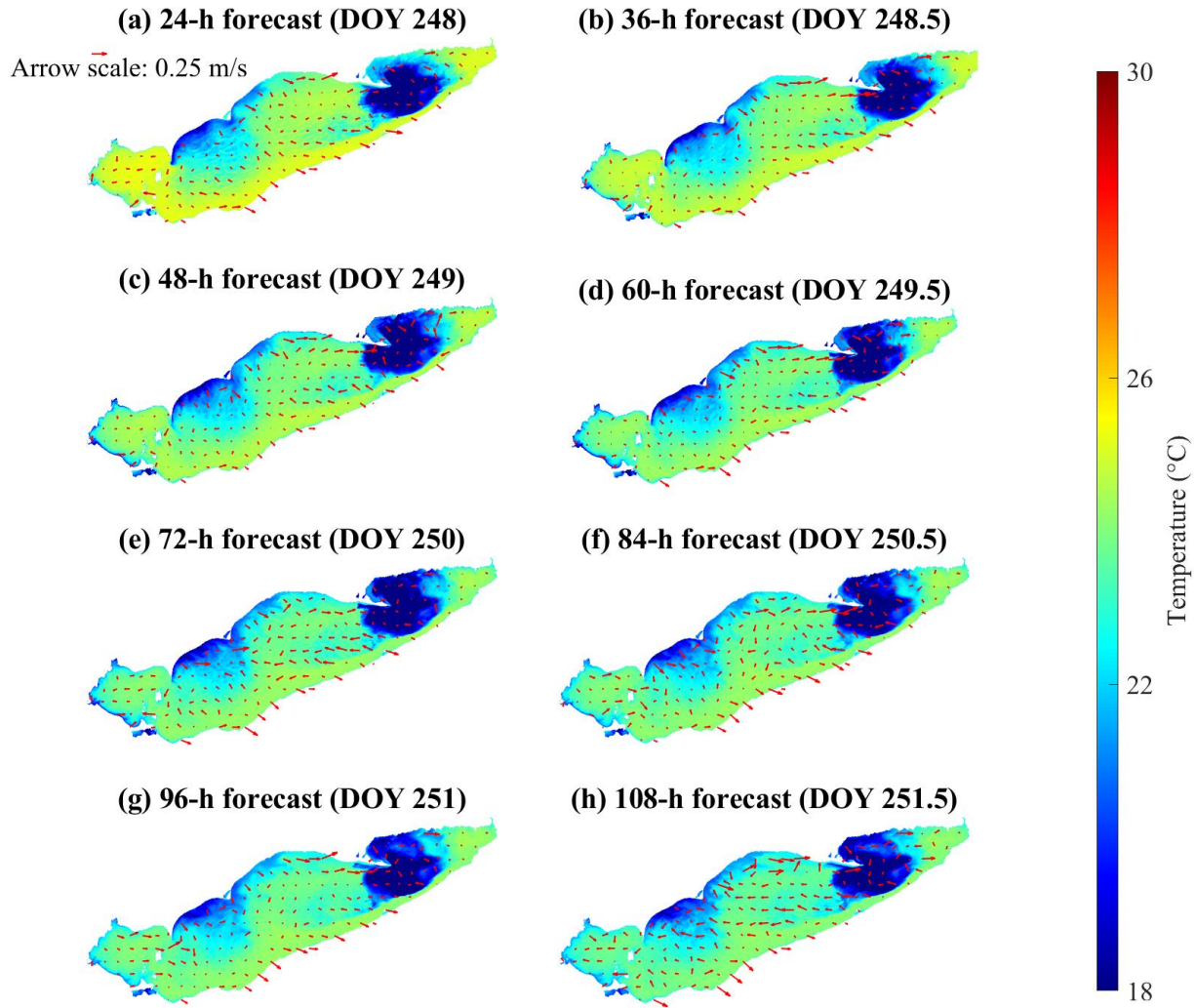
334 4.1 Prediction of coastal up-welling for fishery and drinking water management

335 The central basin of Lake Erie is vulnerable to hypoxia in summer from near-bed thermal stratification and the
 336 relatively large ratio of sediment area to hypolimnetic volume (Bouffard et al., 2013; Nakhaei et al., 2021).
 337 Associated fish kill events (10s of thousands) are regularly reported, including an event on north shore of the central
 338 basin in the late summer of 2012, which was presumably caused by up-welling of cold anoxic water from the
 339 hypolimnion (MOE, 2012; Rao et al., 2014). Similarly, 1000s of freshwater drum were killed in a rapid warming
 340 event (~5 °C /week) in the western basin in 2020 (<https://www.13abc.com/content/news/Hundreds-of-dead-fish->

341 [wash-up-in-Sandusky-Bay-571025541.html](#)). Similarly, shoreward advection of hypoxic water, from up-welling or
342 internal waves also adversely affects source water quality at drinking water intakes (<https://epa.ohio.gov>), whereby
343 high Fe and Mn or low pH, associated with hypoxic water requires adjustment of treatment processes. This is a
344 particular issue along the Ohio coast of the central basin (Ruberg et al., 2008; Rowe et al., 2019).

345 The ability to predict these movements of hypolimnion water would aid management of both Lake Erie
346 fisheries and drinking water treatment. Here, we test the ability of the model to predict up-welling of cold bottom
347 water in the region where the fish kill was observed in 2012. On days 249-253, 2020 (Fig. 8) strong southwesterly
348 winds ($\sim 12 \text{ m s}^{-1}$; Fig. C2) were modelled and observed to create up-welling along the north shore, as expected
349 from Ekman drift of the surface layer (Jabbari et al., 2019). The upwelled cold hypolimnetic water is shown near the
350 coast of Erieau in the satellite observations and the 15 km resolution model (Fig. 8 a, b, e, f). The depth-averaged
351 water temperature and current circulation in the forecast shows up-welling to persist for several days (Fig. 11), with
352 cold hypolimnetic water accumulating along north shore and strong eastward currents along the northern shoreline
353 of the east-central basin. The up-welling region matched that shown in a 2013 hindcast simulation (Valipour et al.,
354 2019), revealing the hotspots of vertical transport of nutrients and anoxic hypolimnetic water.

355 Another up-welling event occurred near the Cleveland drinking water intake crib on days 167-170 (Fig. 9).
356 This event was accompanied by simultaneous $\sim 8 \text{ mg L}^{-1}$ oscillations in the observed dissolved oxygen concentration
357 (Fig. 9 c) at STN 45164 ($\sim 20 \text{ km}$ away from STN 45176), followed by the dissolved oxygen concentration
358 becoming locally hypoxic ($< 2 \text{ mg/L}$) for ~ 2 days. The COASTLINES model predicted this event (section 3.2.2),
359 which would have provided sufficient notice for drinking water plane operators to implement the additional
360 treatment required for hypoxic water (Rowe et al., 2019). Future work, using the coupled iWaterQuality
361 biogeochemical module (formerly CAEDYM) could extend COASTLINES to forecast water quality in Lake Erie
362 (León et al., 2011), including dissolved oxygen concentrations and formation of algae blooms (Bocaniov et al.,
363 2020).



364

365 **Fig. 11** Color maps showing the forecast depth-averaged temperature throughout the lake. The red arrows
 366 represent forecast depth-averaged currents. The model results are from the 240-h forecast model hot-started
 367 on day 247.

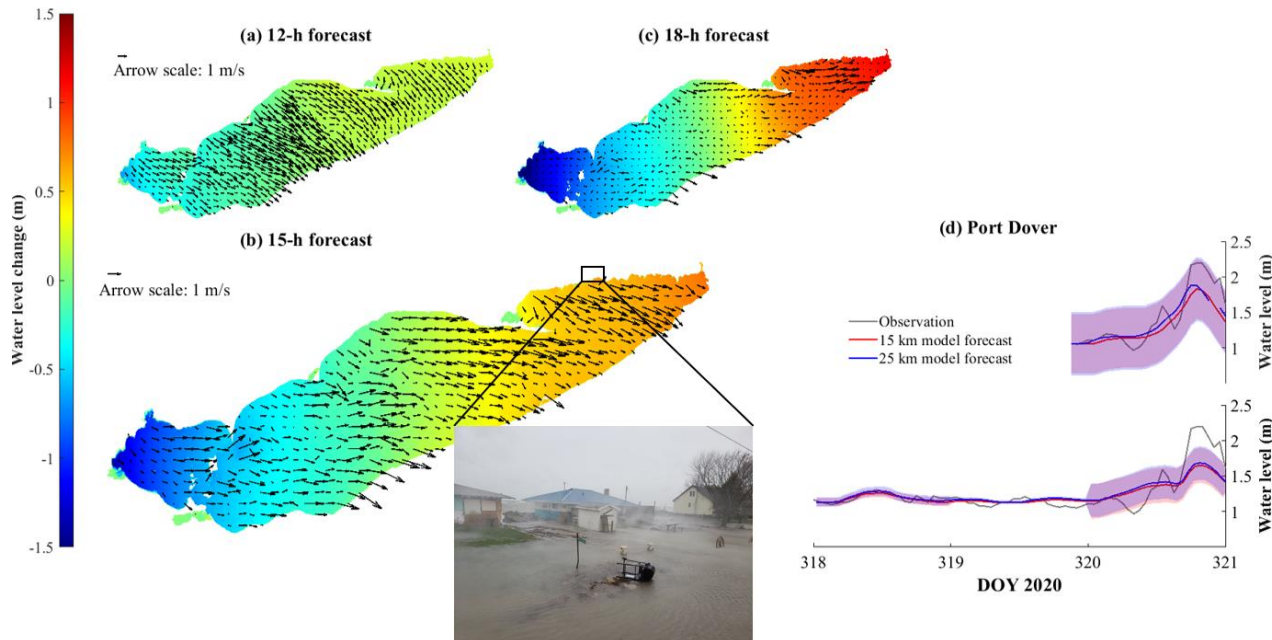
368 **4.2 Prediction of storm surge events for public safety**

369 Due to its shallowness and long fetch aligned with the predominant southwest winds (Hamblin, 1979), Lake Erie has
 370 the largest daily range of water level amongst the Great Lakes (Trebitz, 2006); these water level fluctuations are
 371 mainly due to storm surges and surface seiches (Mortimer, 1987). In every month of 2020, Lake Erie set new mean
 372 water level records (<https://www.tides.gc.ca/C&A/bulletin-eng.html>), causing the shoreline to be exposed to high
 373 risk from erosion and flooding and making the shoreline communities susceptible to costly damage and economic
 374 loss (e.g., <https://www.lowerthames-conservation.on.ca/flood-forecasting/flood-notices/>). Given the ability of
 375 COASTLINES to predict water level fluctuations induced by storm surges and seiches (Fig. 3, 5), we tested the
 376 ability of the model to act as a coastal flooding warning system. Due to the unpredictability and severity of water

377 level fluctuations in Lake Erie, there is currently a need to improve short-term water level forecasts and water level
 378 warning systems (Gronewold and Stow, 2014). This would assist early decision making during natural hazards
 379 (Gronewold and Rood, 2019).

380 We forecast the storm event on 15 Nov. 2020, which generated a wind-induced storm surge (~1-1.5 m) in
 381 the eastern basin with associated strong surface currents (Fig. 12). The inset image, taken during the event, shows
 382 the coastal flooding from this event. COASTLINES successfully predicted the high-water level phase at Port Dover
 383 72 hours in advance, but underestimated the water level increase by 0.5 m. The hot-start forecast 24 hours in
 384 advance was more accurate in predicting the water level prediction, with a difference <0.5 m from the observations
 385 (Fig. 12 d). Note that both forecasts missed the small (~0.5 m) seiche before the significant increase at the end of
 386 day 320, presumably due to the low temporal resolution of the meteorological forecast input or local topography
 387 near the gauge. The overall wind-induced tilt of the free surface was less from the 72 hours hot-start, relative to the
 388 24 hour hot start (Fig. E1), which predicted a larger local storm surge (Fig. 12d).

389 The impacts of coastal flooding could be improved by including simulation of wind-waves through
 390 enabling the coupled surface wave model SWAN (Booij et al., 1999) in AEM3D. Similarly coupled Delft3D-SWAN
 391 models have recently been applied in the development of a real-time predictive system for the coastal ocean and
 392 large estuaries (Rey and Mulligan, 2021).



393
 394 **Fig. 12** Color maps showing the water level change compared to Nov 15th 00h from (a) 12 h, (b) 15 h, and (c)
 395 18 h forecasts from 15 km resolution model. The black arrows are depth-averaged mean current fields. Panel
 396 (d) shows a comparison between forecast and observed water level at Port Dover. The upper panel shows the
 397 forecast hot-started on 15 Nov. 2020 (day 320), and the lower panel shows the forecast hot-started on 12 Nov.
 398 2020 (day 317). The shaded region indicates the confidence interval. The inset image (extracted from a footage
 399 by J. Homewood from Lower Thames Valley Conservation Authority) shows the flooding induced by the
 400 dramatic water level increase during this event. The two cottages shown in the images were destroyed later in
 401 the afternoon.

402 **4.3 Bias and uncertainty**

403 The AEM3D model (formerly ELCOM) employed in COASTLINES has shown skill in temperature hindcasts in the
404 Great Lakes with RMSD $\sim 0.9 - 3$ °C in Lake Erie (Liu et al., 2014; Oveisy et al., 2012) and 1.5 – 1.9 °C in Lake
405 Ontario (Paturi et al., 2012). Similarly, the 24-h COASTLINES forecast predicted water temperatures with an
406 average s-RMSD and t-RMSD < 2 °C at the surface (Table 2). Therefore, the forecasts are within ~ 1 °C RMSD in
407 comparison to hindcasts, showing sufficient model skill for predictive simulations to aid lake management (e.g.,
408 movements of hypoxic water, fish thermal habitat, etc.). The accuracy of the COASTLINES forecasts may result
409 from the high spatial resolution and coverage of meteorological forecast compensating for the inherent inaccuracies
410 in the weather forecast data. Errors in forcing data may be compensated for using data assimilation (Baracchini et
411 al., 2020b). In the hindcast models, Liu et al. (2014) applied uniform Lake Erie meteorological forcing over 4 zones
412 and Valipour et al. (2019) utilized 6 zones, each spanning ~ 100 km. These included land-based observations, when
413 there was no available lake buoy data, which induces error, especially in large shallow lakes (Hamblin, 1987). The
414 comparatively high-resolution GDPS meteorological forecast was four to five times higher in horizontal resolution
415 than used in the hindcast simulations, improving the representation of regional meteorological and climatological
416 conditions.

417 Compared to other operational lake forecast systems, the 240-h COASTLINES forecast is longer (e.g.,
418 GLCFS forecasts 120 hours and meteolakes.ch forecasts 108 hours) and is the only one forced with open-access
419 meteorological data that has global coverage. The GLCFS provided 48-h water level forecasts with RMSD ~ 0.12 m
420 at the Buffalo gauge and ~ 0.14 m at the Toledo gauge, corresponding to RE $\sim 60\%$ and 51%, respectively (O'connor
421 et al., 1999; Trebitz, 2006); using the older 4 km grid Princeton Ocean Model implementation, as opposed to the
422 newer unstructured grid FVCOM GLCFS. COASTLINES gives better 48-h water level forecast performance (RE \sim
423 40 %) at six gauge stations. For temperature, benefitting from a smaller domain, finer resolution meteorological
424 input (~ 2.2 km) and data assimilation, the 4.5-day lake surface temperature predicted by meteolakes.ch has a RMSD
425 = 0.8 °C (Baracchini et al., 2020b), whereas COASTLINES predicted the 120-h (5 d) lake surface temperature with
426 RMSD ~ 1.7 °C. COASTLINES also outperforms 1D climatological hindcasts (e.g., Freshwater Lake (FLake)),
427 with 2– 4 °C RMSD over a 120-h lake surface temperature forecast (Lv et al., 2019; Gu et al., 2015) and has similar
428 error to the 3D Princeton Ocean Model (Kelley et al., 1998), with 0.6-0.9 °C mean absolute error in the 36-h lake
429 surface temperature forecast at station 45005.

430 The uncertainty and bias in the COASTLINES forecast results from error induced by the initial conditions
431 at each hot-start, error in the meteorological forecasts and error in the numerical methods. These errors could be
432 reduced by improving model calibration through data assimilation. For example, Baracchini et al. (2020a) reduced
433 the RMSE temperature simulation of Lake Geneva from ~ 2 °C to ~ 1 °C by employing a data assimilation routine;
434 this would correspond to a $<5\%$ improvement in simulation of Lake Erie summer surface temperature. Before
435 implementing data assimilation, the limitations of such a scheme must be considered: (i) The lack of observations in
436 the future, makes data assimilation impossible for adjusting forecasts; (ii) data assimilation is computationally
437 intensive, required ~ 1 month of computational time (Baracchini et al., 2020a), clearly not an option for operational
438 forecasting); and (iii) data assimilation requires modification of the source code, which is not consistent with our

439 philosophy to develop modelling tools that can be universally applied. Rather, future work will focus on adding real
440 time model calibration (e.g., Gaudard et al. (2019)), which is not presently included in the COASTLINES forecast
441 workflow. For example, Baracchini et al. (2020a) employed OpenDA (<https://www.openda.org/>) as a black-box
442 wrapper to calibrate DELFT3D for Lake Geneva. This approach can be adapted to any other model.

443 The errors induced by hot-starting were shown to be negligible (Fig. 4, 6, 7 (a, b), Fig. A1). However,
444 uncertainty from boundary conditions, especially the meteorological forcing, may introduce error. The 23 to 31
445 meteorological zones from the forecast wind field provides spatial variability required to simulate the mean surface
446 circulation (Laval et al., 2003), water level (Trebitz, 2006), and thermocline motions (Valipour et al., 2015; Valipour
447 et al., 2019). However, the 3-h time interval between GDPS forecast dataset updates is much less than the 10-min
448 interval associated with meteorological data observed at lake-buoys (typically one to six) used to drive hindcasts
449 (e.g., León et al. (2005)) and so the coarse temporal resolution in GDPS forecast may alias temporal events, such as
450 wind gusts (Fig. C1). This is of particular concern in large shallow lakes, such as Lake Erie, where winds play the
451 dominant role in driving hydrodynamics. The rapid response of the water level to windstorms (Hamblin, 1987)
452 could result in the effects of aliasing and forecast error being passed to the water level, leading to the growth of RE
453 against forecast time (Fig. 3). The meteorological forecast from the 15 km and 25 km GDPS models did not show
454 discrepancies (Fig. C2-5) and the evaluation metrics indicate that forecast results were largely insensitive to the
455 meteorological inputs in Lake Erie (Fig. 3, 7). However, the 15 km model better predicted the mesoscale upwelling
456 event (Fig. 8, 9, D2). The 24-h air temperature and wind speed forecasts had ~ 1.5 °C and ~ 2 m s $^{-1}$ RMSD,
457 respectively. However, bias in the 240-h forecast increases with forecast time (Buehner et al., 2015). The 168-h
458 forecast meteorological data overestimated wind speeds by up to 10 m s $^{-1}$ (Fig. C4), and bias in the air temperature
459 forecast (Fig. C5) may cause the consistent warm bias (up to 3°C) in forecast lake surface temperature (Fig. 8).
460 These errors may be corrected through real time calibration using data assimilation (Baracchini et al., 2020a, b). The
461 growing bias in air temperature, with forecast time, does not affect the lake surface temperature (Fig. 7), presumably
462 owing to the buffer effect of surface mixing layer (Schertzer et al., 1987).

463 Neglecting the inflows and outflows in the predictive simulation could induce bias in the forecast. The
464 overestimation of water level fluctuation range near Bar Point (Fig. 4f) may result from neglecting the large Detroit
465 River inflow, which regulates the seiche magnitude. The inflows also adjust more rapidly to air temperatures
466 compared to deep lake waters. Thus, the up to 2 °C cold bias in coastal regions of the western basin (Fig. 8 m-t, Fig.
467 D2) could be induced by neglecting the heated flux from two major inflows (i.e., Detroit River and Maumee River)
468 of Lake Erie.

469 In addition to inaccuracy in initial and boundary conditions, the discrepancies in simulating temperature
470 profiles forecast may result from numerical diffusion arising due to the discrete nature of the vertical and horizontal
471 grids. The simulated thermocline depth is overestimated (Fig. 9, 10), as occurred in applications of ELCOM with
472 both higher (Nakhaei et al., 2019) and lower resolution (Paturi et al., 2012). COASTLINES has the potential to
473 predictively simulate mesoscale physical processes, such as Kelvin waves (Bouffard and Lemmin, 2013) and
474 nearshore-offshore exchange (Valipour et al., 2019); however, model performance is poor in nearshore areas, where
475 topographic features remain poorly resolved.

476 **5 Conclusions**

477 We developed an operational forecast system COASTLINES, using the Windows Task Scheduler, Python-based
478 data scrapping/formatting, and MATLAB data processing scripts, to automate application of a black-box
479 hydrodynamic driver (AEM3D) to Lake Erie as an operational forecast tool. The resulting real-time and predictive
480 lake modelling system used meteorological forecasts to generate 240-h forecasts of the lake surface level and 3D
481 temperature and current fields on a 500 m × 500 m (horizontal) × ~ 1 m (vertical) grid, compares model output with
482 near real time observations and publishes the model output on a web-based platform.

483 The favorable agreement between forecast model results and observed physical variables (e.g., water level
484 RE ~ 40 % and temperature t-RMSD and s-RMSD < 2 °C) in Lake Erie demonstrates the ability of the forecast
485 system to make predictions of hydrodynamic processes on time horizons up to 240-h that are as accurate as
486 traditional hindcast simulations using directly observed meteorological forcing. This enables the near real-time
487 updates to the web platform to be used as a communication tool that rapidly disseminate forecast results to managers
488 and stakeholders. Examples include >24-h prediction of: (i) up- and down-welling events leading to fish kills; (ii)
489 up-welling events transporting hypoxic water to a drinking water intake; and (iii) coastal flooding events from storm
490 surges.

491 This operational system shows the feasibility of applying freely available meteorological forecasts (e.g.,
492 GDPS, HRRR), in situ buoy data and satellite images to drive and validate any computational lake model (e.g.,
493 AEM3D, DELFT3D, GLM), without modifying the source code. The global coverage of the weather model allows
494 generalization of model application to any lake or coastal domain. To facilitate further development of open-access
495 predictive modelling systems, agencies are encouraged to share model validation observations, in real-time, through
496 organizations such as GLEON (www.gleon.org) and GLOS (www.glos.us). This will enable extension of
497 COASTLINES to include prediction of the physical-biogeochemical variables that drive sediment transport,
498 hypoxia, and harmful algal blooms.

499

500 **Code and data availability.**

501 The observed data and meteorological forcing used in this study is openly accessible online as cited in the text. The
502 COASTLINES model output is archived on the server and can be obtained by contacting the corresponding author.
503 The Python and MATLAB scripts as well as the timeline set in Windows Task Scheduler are archived in the
504 Scholars Portal Dataverse (<https://doi.org/10.5683/SP2/VTN7WC>, Lin, 2021). The AEM3D executable was used as
505 a black box hydrodynamic transport code. The executable used in COASTLINES is available for a nominal license
506 fee from Hydronumerics (<https://www.hydronumerics.com.au/>). The AEM3D source code was not modified
507 in this application but is available with permission from Hydronumerics.

508 **Author contributions.**

509 The concept of the COASTLINES workflow was designed by LB, SL, SS, and RM, and SL carried them out. SL
510 developed the model code and performed the simulations. All authors contributed to the validation of the model and
511 interpretation of the results. SL wrote the manuscript with contributions from LB, SS, and RM.

512 **Acknowledgements.**

513 This project was funded by the Dean's Research Fund from the Faculty of Engineering and Applied Science at
514 Queen's University. Computational support was provided by Alexander Rey and FEAS-ITS. LB thanks Damien
515 Bouffard for discussions during visits to EAWAG, which inspired this research. James Homewood, from the Lower
516 Thames Valley Conservation Authority (LTVCA) providing footages of the storm event on Nov. 15th, 2020.

517 **Reference**

518 Anderson, E. J., Fujisaki-Manome, A., Kessler, J., Lang, G. A., Chu, P. Y., Kelly, J. G. W., Chen, Y., and Wang, J.:
519 Ice forecasting in the next-generation Great Lakes Operational Forecast System (GLOFS), *J. Mar. Sci. Eng.*, 6,
520 10.3390/jmse6040123, 2018.

521 Antenucci, J., and Imerito, A.: The CWR dynamic reservoir simulation model DYRESM, *Science Manual*, The
522 University of Western Australia, Perth, Australia, 2000.

523 Baracchini, T., Hummel, S., Verlaan, M., Cimatoribus, A., Wüest, A., and Bouffard, D.: An automated calibration
524 framework and open source tools for 3D lake hydrodynamic models, *Environmental Modelling & Software*, 134,
525 104787, 2020a.

526 Baracchini, T., Wüest, A., and Bouffard, D.: Meteolakes: An operational online three-dimensional forecasting
527 platform for lake hydrodynamics, *Water Res.*, 172, 10.1016/j.watres.2020.115529, 2020b.

528 Beletsky, D., Hawley, N., Rao, Y. R., Vanderploeg, H. A., Beletsky, R., Schwab, D. J., and Ruberg, S. A.: Summer
529 thermal structure and anticyclonic circulation of Lake Erie., *Geophys. Res. Lett.*, 39, 10.1029/2012GL051002, 2012.

530 Bocaniov, S. A., and Scavia, D.: Temporal and spatial dynamics of large lake hypoxia: Integrating statistical and
531 three-dimensional dynamic models to enhance lake management criteria, *Water Resour. Res.*, 52, 4247-4263,
532 10.1002/2015WR018170, 2016.

533 Bocaniov, S. A., Lamb, K. G., Liu, W., Rao, Y. R., and Smith, R. E.: High sensitivity of lake hypoxia to air
534 temperatures, winds, and nutrient loading: Insights from a 3-D lake model, *Water Resources Research*, 56,
535 e2019WR027040, 2020.

536 Boegman, L., Loewen, M. R., Hamblin, P., and Culver, D.: Application of a two-dimensional hydrodynamic
537 reservoir model to Lake Erie, *Canadian Journal of Fisheries and Aquatic Sciences*, 58, 858-869, 2001.

538 Boegman, L., Loewen, M., Hamblin, P. F., and A., C. D.: Vertical mixing and weak stratification over zebra mussel
539 colonies in western Lake Erie, *Limnol. Oceanogr.*, 53, 1093-1110, 10.4319/lo.2008.53.3.1093, 2008.

540 Booij, N., Ris, R. C., and Holthuijsen, L. H.: A third-generation wave model for coastal regions 1. Model description
541 and validation *J. Geophys. Res. Oceans*, 104, 7649–7666, 10.1029/98JC02622, 1999.

542 Bouffard, D., Boegman, L., and Rao, Y. R.: Poincaré wave-induced mixing in a large lake, *Limnology and
543 oceanography*, 57, 1201-1216, 2012.

544 Bouffard, D., Ackerman, J. D., and Boegman, L.: Factors affecting the development and dynamics of hypoxia in a
545 large shallow stratified lake: hourly to seasonal patterns, *Water Resources Research*, 49, 2380-2394, 2013.

546 Bouffard, D., and Lemmin, U.: Kelvin waves in Lake Geneva, *J. Great Lakes Res.*, 39, 637-645,
547 10.1016/j.jglr.2013.09.005, 2013.

548 Bouffard, D., Boegman, L., Ackerman, J. D., Valipour, R., and Rao, Y. R.: Near-inertial wave driven dissolved
549 oxygen transfer through the thermocline of a large lake, *J. Great Lakes Res.*, 40, 300-307,
550 10.1016/j.jglr.2014.03.014, 2014.

551 Brookes, J. D., and Carey, C. C.: Resilience to blooms, *Science*, 334, 46-47, 10.1126/science.1207349, 2011.

552 Buehner, M., McTaggart-Cowan, R., Beaulne, A., Charette, C., Garand, L., Heilliette, S., Lapalme, E., Laroche, S.,
553 Macpherson, S. R., Morneau, J., and Zadra, A.: Implementation of deterministic weather forecasting systems based
554 on ensemble-variational data assimilation at Environment Canada. Part I: the global system, *Mon. Wea. Rev.*, 143,
555 2532-2559, 10.1175/MWR-D-14-00354.1, 2015.

556 Caramatti, I., Peeters, F., Hamilton, D., and Hofmann, H.: Modelling inter-annual and spatial variability of ice cover
557 in a temperate lake with complex morphology, *Hydrol. Process.*, 34, 691-704, 10.1002/hyp.13618, 2019.

558 Casulli, V., and Cheng, R.: Semi-implicit finite difference methods for three-dimensional shallow water flow. , *Int.
559 J. Numer. Methods Fluids* 15, 629-648, 10.1002/fld.1650150602 1992.

560 Chen, C., Beardsley, R. C., Cowles, G., Qi, J., Lai, Z., Gao, G., Stuebe, D., Xu, Q., Xue, P., Ge, J., Ji, R., Tian, R.,
561 Huang, H., Wu, L., and Lin, H.: An unstructured grid, finite-volume community ocean model FVCOM user manual,
562 SMAST/UMASSD Tech. Rep. 11-1101, 373 pp., Dartmouth, Mass., 2012.

563 Chu, P. Y., Kelley, J. G. W., Mott, G. V., Zhang, A., and Lang, G. A.: Development, implementation, and skill
564 assessment of the NOAA/NOS Great Lakes Operational Forecast System, *Ocean Dyn.* , 61, 1305-1316,
565 10.1007/s10236-011-0424-5, 2011.

566 Gaudard, A., Schwefel, R., Vinnå, L. R., Schmid, M., Wüest, A., and Bouffard, D.: Optimizing the parameterization
567 of deep mixing and internal seiches in one-dimensional hydrodynamic models: a case study with Simstrat v1.3,
568 *Geosci. Model Dev.*, 10, 3411-3423, 10.5194/gmd-10-3411-2017, 2017.

569 Gaudard, A., Vinnå, L. R., Bärenbold, F., Schmid, M., and Bouffard, D.: Toward an open-access of high-frequency
570 lake modelling and statistics data for scientists and practitioners. The case of Swiss Lakes using Simstrat v2.1,
571 *Geosci. Model Dev.*, 12, 3955-3974, 10.5194/gmd-2018-336, 2019.

572 Gronewold, A. D., and Rood, R. B.: Recent water level changes across Earth's largest lake system and implications
 573 for future variability, *J. Great Lakes Res.*, 45, 1-3, 10.1016/j.jglr.2018.10.012, 2019.

574 Gu, H., Jin, J., Wu, Y., Ek, M. B., and Subin, Z. M.: Calibration and validation of lake surface temperature
 575 simulations with the coupled WRF-lake model, *Climatic Change*, 129, 471-483, 2015.

576 Hamblin, P. F.: Great Lakes storm surge of April 6, 1979, *J. Great Lakes Res.*, 5, 312-315, 10.1016/S0380-
 577 1330(79)72157-5, 1979.

578 Hamblin, P. F.: Meteorological forcing and water level fluctuations on Lake Erie, *J. Great Lakes Res.*, 13, 436-453,
 579 10.1016/S0380-1330(87)71665-7, 1987.

580 Hecky, R. E., Smith, R. E. H., Barton, D. R., Guildford, S. J., Taylor, W. D., Charlton, M. N., and Howell, T.: The
 581 nearshore phosphorus shunt: a consequence of ecosystem engineering by dreissenids in the Laurentian Great Lakes,
 582 *Can. J. Fish. Aquat. Sci.*, 61, 1285-1293, 10.1139/F04-065, 2004.

583 Higgins, S. N., Hecky, R. E., and Guildford, S. J.: Environmental controls of cladophora growth dynamics in eastern
 584 Lake Erie: Application of the Cladophora Growth Model (CGM), *J. Great Lakes Res.*, 32, 629-644, 10.3394/0380-
 585 1330(2006)32[629:ECOCGD]2.0.CO;2, 2006.

586 Hipsey, M. R., Bruce, L. C., and Hamilton, D. P.: GLM - General Lake Model. Model overview and user
 587 information, Technical Manual, The University of Western Australia, Perth, Australia., 2014.

588 Hodges, B. R., Imberger, J., Saggio, A., and Winters, K. B.: Modeling basin-scale internal waves in a stratified lake,
 589 *Limnology and Oceanography*, 45, 1603-1620, 10.4319/lo.2000.45.7.1603, 2000.

590 Jabbari, A., Ackerman, J. D., Boegman, L., and Zhao, Y.: Episodic hypoxia in the western basin of Lake Erie,
 591 *Limnology and Oceanography*, 64, 2220-2236, 2019.

592 Jabbari, A., Ackerman, J. D., Boegman, L., and Zhao, Y.: Increases in Great Lake winds and extreme events
 593 facilitate interbasin coupling and reduce water quality in Lake Erie, *Scientific Reports*, 11, 5733, 10.1038/s41598-
 594 021-84961-9, 2021.

595 Kelley, J. G. W., Hobgood, J. S., Bedford, K. W., and Schwab, D. J.: Generation of Three-Dimensional Lake Model
 596 Forecasts for Lake Erie, *Weather and Forecasting*, 13, 659-687, 10.1175/1520-
 597 0434(1998)013<0659:GOTDLM>2.0.CO;2, 1998.

598 Laval, B., Imberger, J., Hodges, B. R., and Stocker, R.: Modeling circulation in lakes: Spatial and temporal
 599 variations, *Limnology and oceanography*, 48, 983-994, 2003.

600 León, L. F., Imberger, J., Smith, R. E. H., Hecky, R. E., Lam, D. C. L., and Schertzer, W. M.: Modeling as a tool for
 601 nutrient management in Lake Erie: a hydrodynamics study, *J. Great Lakes Res.*, 31, 309-318, 10.1016/S0380-
 602 1330(05)70323-3, 2005.

603 León, L. F., Smith, R. E. H., Hipsey, M. R., Bocaniov, S. A., Higgins, S. N., Hecky, R. E., Antenucci, J. P.,
 604 Imberger, J. A., and Guildford, S. J.: Application of a 3D hydrodynamic-biological model for seasonal and spatial
 605 dynamics of water quality and phytoplankton in Lake Erie, *J. Great Lakes Res.*, 37, 41-53,
 606 10.1016/j.jglr.2010.12.007, 2011.

607 Leonard, B. P.: The ULTIMATE conservative difference scheme applied to unsteady one-dimensional advection.,
 608 *Comp. Methods Appl. Mech. Eng.*, 88, 17-74, 1991.

609 Lesser, G. R., Roelvink, J. V., Van Kester, J. A. T. M., and Stelling, G. S.: Development and validation of a three-
 610 dimensional morphological model., *Coastal Engineering*, 51, 883-915, 10.1016/j.coastaleng.2004.07.014, 2004.

611 Liu, W., Bocaniov, S. A., Lamb, K. G., and Smith, R. E. H.: Three dimensional modeling of the effects of changes
 612 in meteorological forcing on the thermal structure of Lake Erie, *J. Great Lakes Res.*, 40, 827-840,
 613 10.1016/j.jglr.2014.08.002, 2014.

614 Loewen, M., Ackerman, J. D., and Hamblin, P. F.: Environmental implications of stratification and turbulent mixing
 615 in a shallow lake basin, *Can. J. Fish. Aquat. Sci.*, 64, 43-57, 10.1139/F06-165, 2007.

616 Lv, Z., Zhang, S., Jin, J., Wu, Y., and Ek, M. B.: Coupling of a physically based lake model into the climate forecast
 617 system to improve winter climate forecasts for the Great Lakes region, *Climate Dynamics*, 53, 6503-6517,
 618 10.1007/s00382-019-04939-2, 2019.

619 Madani, M., Seth, R., León, L. F., Valipour, R., and McCrimmon, C.: Three dimensional modelling to assess
 620 contributions of major tributaries to fecal microbial pollution of lake St. Clair and Sandpoint Beach, *J. Great Lakes
 621 Res.*, 46, 159-179, 10.1016/j.jglr.2019.12.005, 2020.

622 Meyers, T., and Dale, R.: Predicting daily insolation with hourly cloud height and coverage, *Journal of Applied
 623 Meteorology and Climatology*, 22, 537-545, 1983.

624 Michalak, A. a. M., Anderson, E. J., Beletsky, D., Boland, S., Bosch, N. S., Bridgeman, T. B., Chaffin, J. D., Cho,
 625 K., Confesor, R., Daloğlu, I., DePinto, J. V., Evans, M. A., Fahnenstiel, G. L., He, L., Ho, J. C., Jenkins, L.,
 626 Johengen, T. H., Kuo, K. C., LaPorte, E., Liu, X., McWilliams, M. R., Moore, M. R., Posselt, D. J., Richards, R. P.,
 627 Scavia, D., Steiner, A. L., Verhamme, E., Wright, D. M., and Zagorski, M. A.: Record-setting algal bloom in Lake

628 Erie caused by agricultural and meteorological trends consistent with expected future conditions, Proceedings of the
629 National Academy of Sciences, 110, 6448-6452, 10.1073/pnas.1216006110, 2013.

630 MOE: Lake Erie fish kill incident on September 1, 2012. Summary Report.Ontario Ministry of the Environment
631 Southwestern Region 14 ((Available from OntarioMinistry of Environment).), 2012.

632 Mortimer, C. H.: Fifty Years of Physical Investigations and Related Limnological Studies on Lake Erie, 1928–1977,
633 Journal of Great Lakes Research, 13, 407-435, 10.1016/S0380-1330(87)71664-5, 1987.

634 Nakhaei, N., Boegman, L., Mehdizadeh, M., and Loewen, M.: Hydrodynamic modeling of Edmonton storm-water
635 ponds, Environ. Fluid Mech., 19, 305-327, 10.1007/s10652-018-9625-5, 2019.

636 Nakhaei, N., Ackerman, J. D., Bouffard, D., Rao, Y. R., and Boegman, L.: Empirical modeling of hypolimnion and
637 sediment oxygen demand in temperate Canadian lakes, Inland Waters, 1-17, 2021.

638 O'Reilly, C. M., Sharma, S., Gray, D. K., Hampton, S. E., Read, J. S., and Rowley, R. J., et al.: Rapid and highly
639 variable warming of lake surface waters around the globe, Geophys. Res. Lett., 42, 10773-10781,
640 10.1002/2015GL066235., 2015.

641 O'Connor, W. P., Schwab, D. J., and Lang, G. A.: Forecast verification for Eta Model winds using Lake Erie storm
642 surge water levels, Weather and forecasting, 14, 119-133, 1999.

643 O'Neil, J. M., Davis, T. W., Burford, M. A., and Gobler, C. J.: The rise of harmful cyanobacteria blooms: The
644 potential roles of eutrophication and climate change, Harmful Algae, 14, 313-334, 10.1016/j.scitotenv.2011.02.001,
645 2012.

646 Oveisy, A., Boegman, L., and Imberger, J.: Three-dimensional simulation of lake and ice dynamics during winter,
647 limnol. Oceanogr., 57, 42-57, 10.4319/lo.2012.57.1.0043, 2012.

648 Paerl, H. W., and Paul, V. J.: Climate change: Links to global expansion of harmful cyanobacteria, Water Research, 46, 1349-1363, 10.1016/j.watres.2011.08.002, 2012.

649 Paturi, S., Boegman, L., and Rao, Y. R.: Hydrodynamics of eastern Lake Ontario and the upper St. Lawrence River,
650 J. Great Lakes Res., 38, 194-204, 10.1016/j.jglr.2011.09.008, 2012.

651 Rao, Y. R., and Murthy, C. R.: Coastal boundary layer characteristics during summer stratification in Lake Ontario.,
652 J. Phys. Oceanogr., 31, 1088-1104, 10.1175/1520-0485(2001)031<1088:CBLCDS>2.0.CO;2, 2001.

653 Rao, Y. R., Hawley, N., Charlton, M. N., and Schertzer, W. M.: Physical processes and hypoxia in the central basin
654 of Lake Erie, Limnol. Oceanogr., 53, 2007-2020, 10.4319/lo.2008.53.5.2007, 2008.

655 Rao, Y. R., Howell, T., Watson, S. B., and Abernethy, S.: On hypoxia and fish kills along the north shore of Lake
656 Erie, J. Great Lakes Res., 40, 187-191, 10.1016/j.jglr.2013.11.007, 2014.

657 Rey, A., and Mulligan, R. P.: Influence of Hurricane Wind Field Variability on RealTime Forecast Simulations of
658 the Coastal Environment, J. Geophys. Res. Oceans, 126, 10.1029/2020JC016489, 2021.

659 Rowe, M. D., Anderson, E. J., Beletsky, D., Stow, C. A., Moegling, S. D., and Chaffin, J. D., et al: Coastal
660 upwelling influences hypoxia spatial patterns and nearshore dynamics in Lake Erie., J. Geophys. Res. Oceans, 124,
661 10.1029/2019JC015192, 2019.

662 Ruberg, S. A., Guasp, E., Hawley, N., Muzzi, R. W., Brandt, S. B., and Vanderploeg, H. A., et al.: Societal benefits
663 of the Real-time Coastal Observation Network (ReCON): Implications for municipal drinking water quality., Mar.
664 Technol. Soc. J., 42, 103-109, 10.4031/002533208786842471, 2008.

665 Saber, A., James, D. E., and Hannoun, I. A.: Effects of lake water level fluctuation due to drought and extreme
666 winter precipitation on mixing and water quality of an alpine lake, Case Study: Lake Arrowhead, California, Sci.
667 Total Environ., 714, 10.1016/j.scitotenv.2020.136762, 2020.

668 Scavia, D., Allan, J. D., Arend, K. K., Bartell, S., Beletsky, D., Bosch, N. S., Brandt, S. B., Briland, R. D., Daloglu,
669 I., DePinto, J. V., Dolan, D. M., and Evans, M. A. e. a.: Assessing and addressing the re-eutrophication of Lake Erie:
670 Centralbasin hypoxia, J. Great Lakes Res., 40, 226-246, 10.1016/j.jglr.2014.02.004, 2014.

671 Scavia, D., DePinto, J. V., and Bertani, I.: A multi-model approach to evaluating target phosphorus loads for Lake
672 Erie, J. Great Lakes Res., 42, 1139-1150, 10.1016/j.jglr.2016.09.007, 2016.

673 Schertzer, W. M., Saylor, J. H., Boyce, F. M., Robertson, D. G., and Rosa, F.: Seasonal Thermal Cycle of Lake Erie,
674 Journal of Great Lakes Research, 13, 468-486, 10.1016/S0380-1330(87)71667-0, 1987.

675 Schwab, D. J., and Beletsky, D.: Propagation of kelvin waves along irregular coastlines in finite-difference models.,
676 Adv. Water Resour., 22, 239-245, 10.1016/S0309-1708(98)00015-3, 1998.

677 Schwab, D. J., Leshkevich, G. A., and Muhr, G. C.: Automated Mapping of Surface Water Temperature in the Great
678 Lakes, J. Great Lakes Res., 25, 468-481, 10.1016/S0380-1330(99)70755-0, 1999.

679 Trebitz, A. S.: Characterizing seiche and tide-driven daily water level fluctuations affecting coastal ecosystems of
680 the Great Lakes, J. Great Lakes Res., 32, 102-116, 10.3394/0380-1330(2006)32[102:CSATDW]2.0.CO;2, 2006.

681 Valipour, R., Bouffard, D., Boegman, L., and Rao, Y. R.: Near-inertial waves in Lake Erie, Limnol. Oceanogr., 60,
682 1522–1535, 10.1021/es301422r, 2015.

683

684 Valipour, R., Rao, Y. R., León, L. F., and Depew, D.: Nearshore-offshore exchanges in multi-basin coastal waters:
685 Observations and three-dimensional modeling in Lake Erie, *J. Great Lakes Res.*, 45, 50-60,
686 10.1016/j.jglr.2018.10.005, 2019.

687 Wang, Q., and Boegman, L.: Multi-Year Simulation of Western Lake Erie Hydrodynamics and Biogeochemistry to
688 Evaluate Nutrient Management Scenarios, *Sustainability*, 13, 7516, 2021.

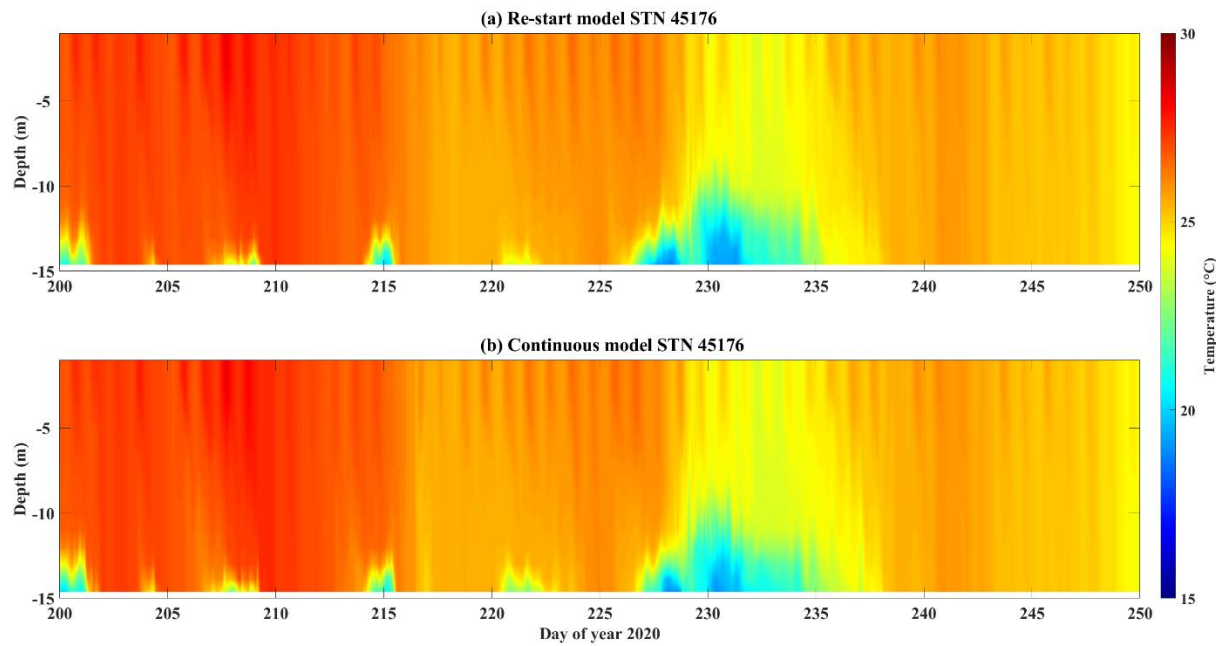
689 Watson, S. B., Miller, C., Arhonditsis, G., Boyer, G. L., and al, e.: The re-eutrophication of Lake Erie: Harmful algal
690 blooms and hypoxia, *Harmful Algae*, 56, 44-66, 10.1016/j.hal.2016.04.010, 2016.

691 Woolway, R. I., and Merchant, C. J.: Worldwide alteration of lake mixing regimes in response to climate change.,
692 *Nat. Geosci.*, 12, 271-276, 10.1038/s41561-019-0322-x, 2019.

693 Woolway, R. I., Kraemer, B. M., and Lengers, J. D., et al.: Global lake responses to climate change, *Nat Rev Earth*
694 *Environ.*, 10.1038/s43017-020-0067-5, 2020.

695

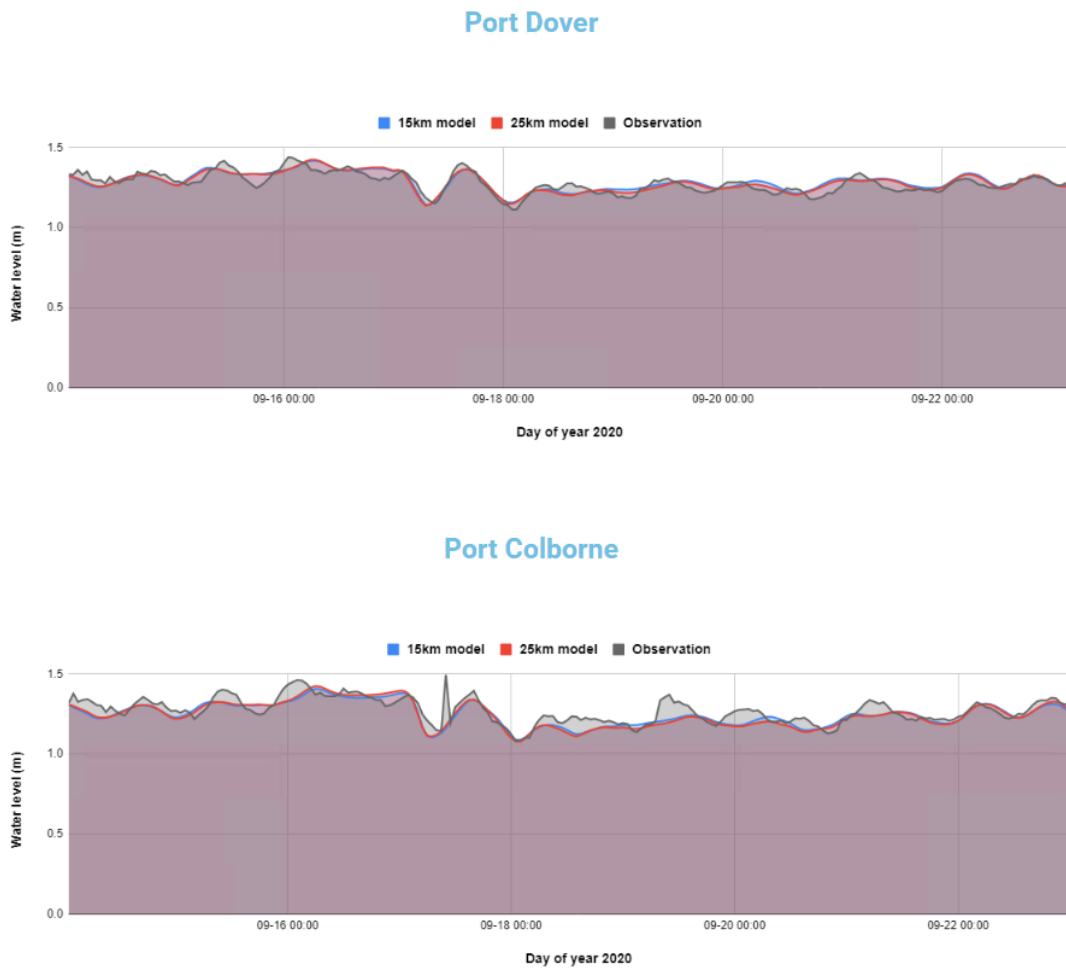
696 **Appendix A: Comparison of 24 h model run with re-start files and model run with continuous files.**



697
698 **Fig. A1 Temperature profile comparison between (a) stitched 24 h model run with re-start files, and (b) model**
699 **run with continuous input files.**

700

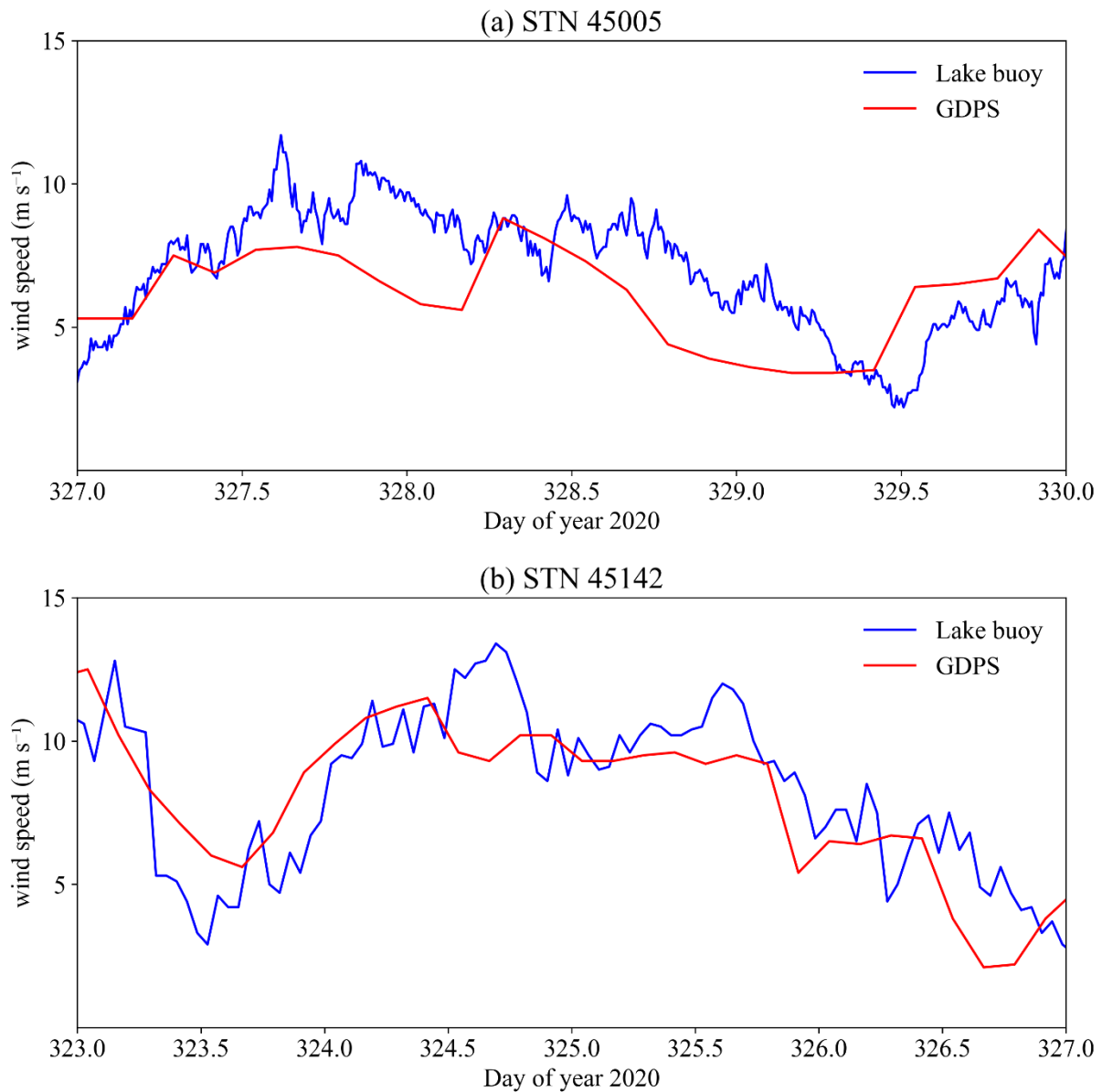
701 **Appendix B: COASTLINE website snapshot**

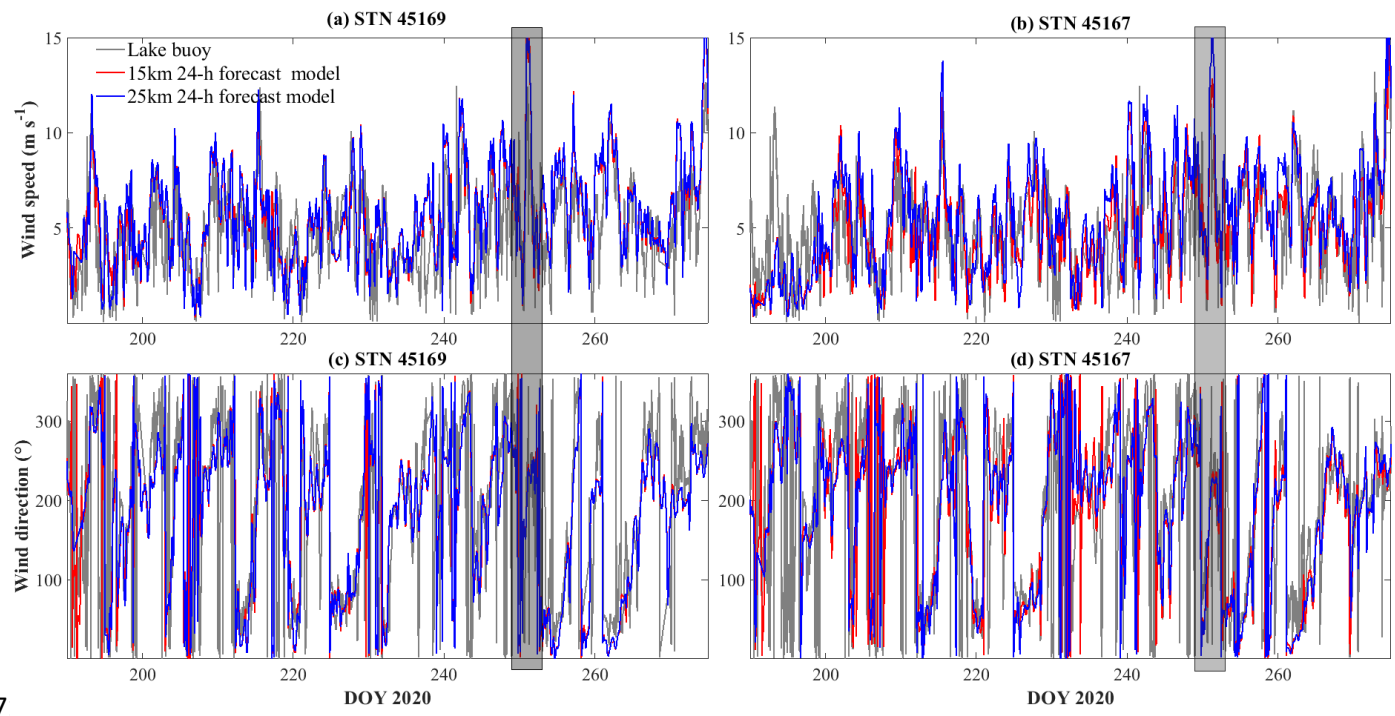


702

703 **Fig. B1 Snapshot of water level forecast validation web page displayed on COASTLINES online platform:**
704 <https://coastlines.engineering.queensu.ca/erie/water-level-forecast>. Status on Sep 23rd, 2020.

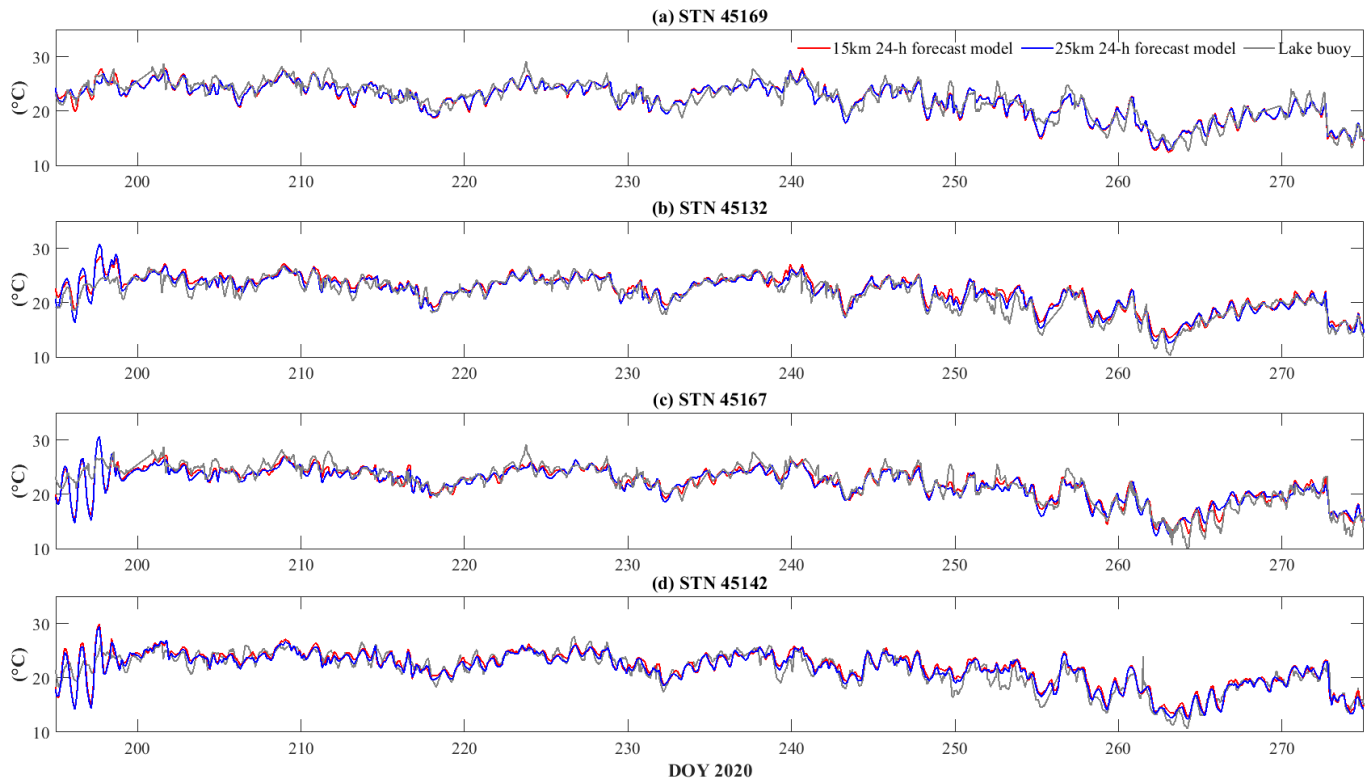
705





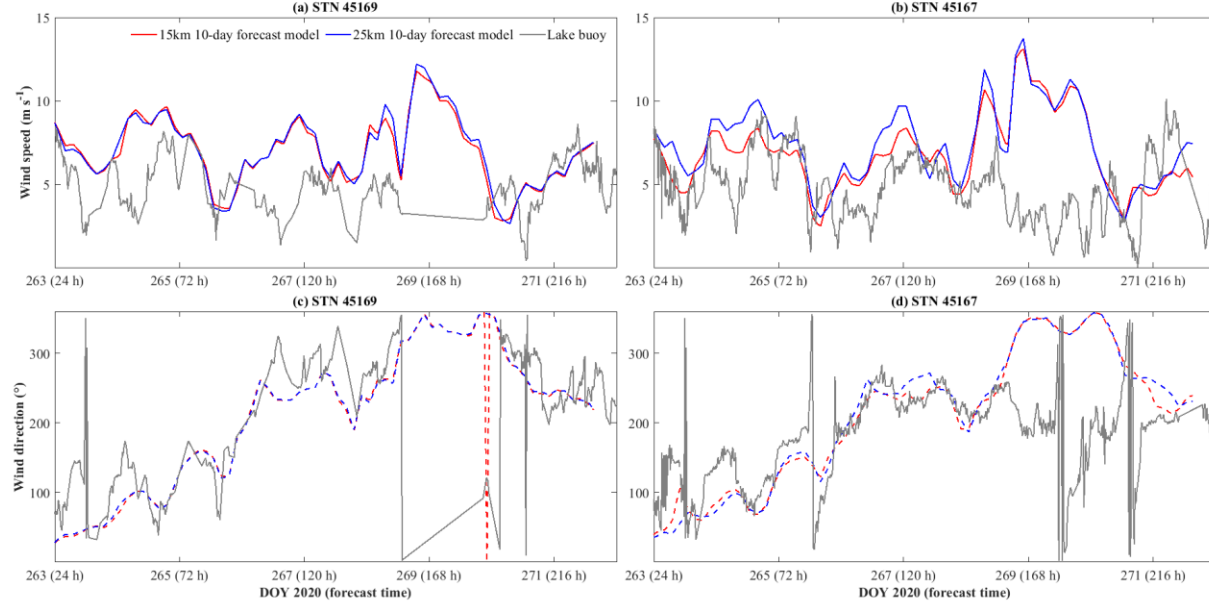
7

712 **Fig. C2 Comparisons of 24-h meteorological forecast and lake buoy observations of wind speed (a, b) and wind**
 713 **direction (c, d). The gray rectangle indicates the storm that led to up-welling along northern shoreline on days**
 714 **248-253.**



7

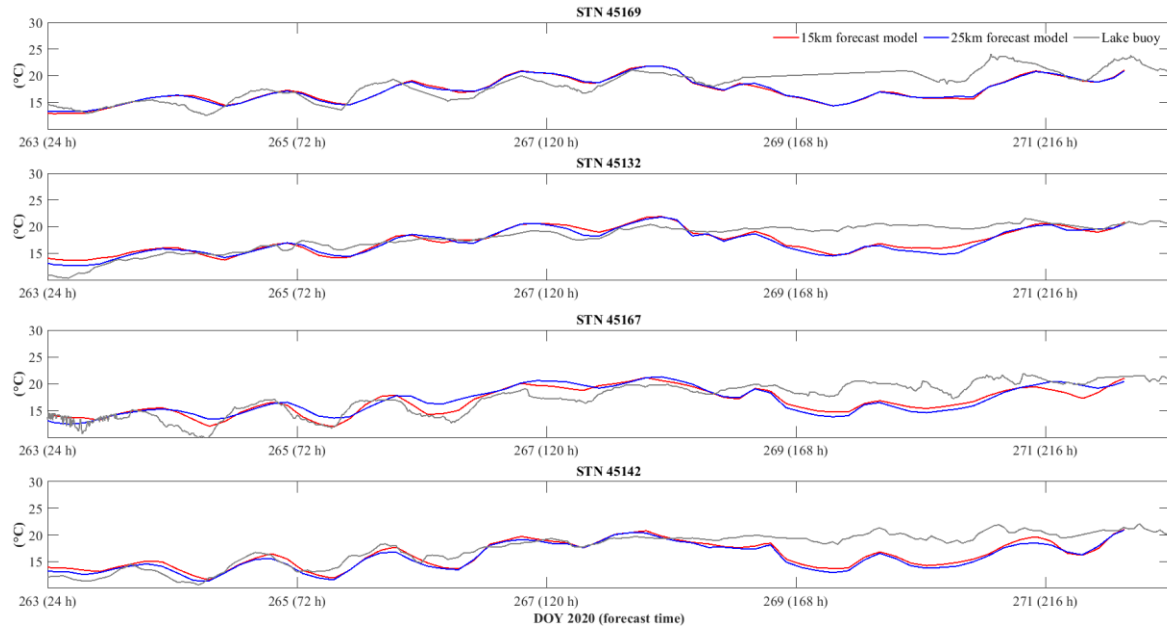
716 **Fig. C3 Comparisons of 24-h air temperature forecast and lake buoy observations of air temperature.**



717

718 **Fig. C4 Comparisons of 240-h meteorological forecast and lake buoy observations of wind speed (a, b) and wind**
 719 **direction (c, d).**

720

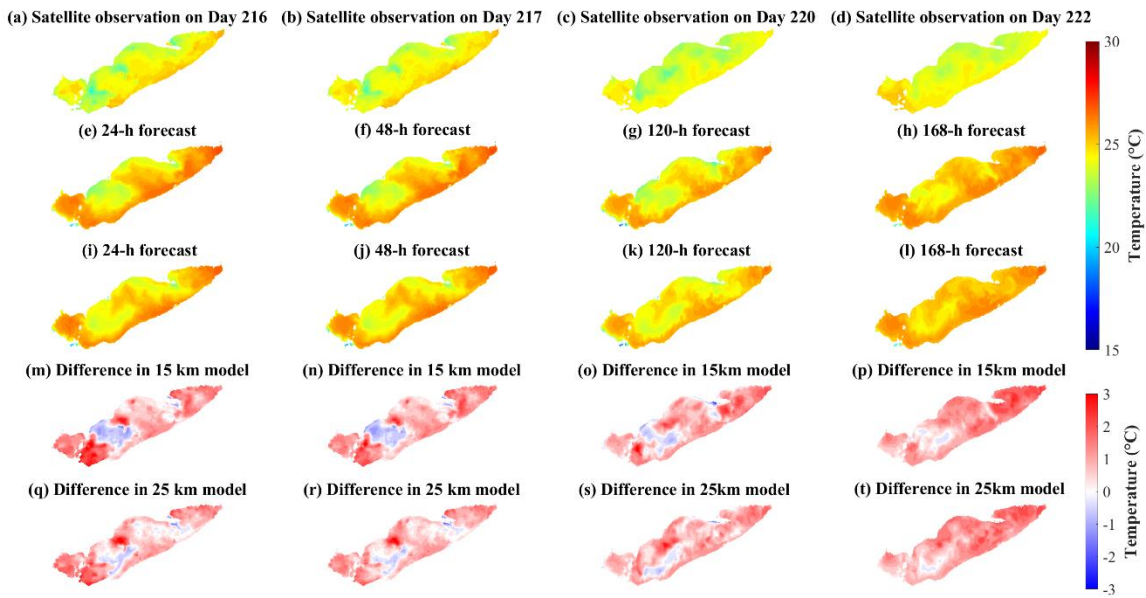


721

722 **Fig. C5 Comparisons of 240-h air temperature forecast and lake buoy observations.**

723 **Appendix D: Temperature validation against satellite observations**

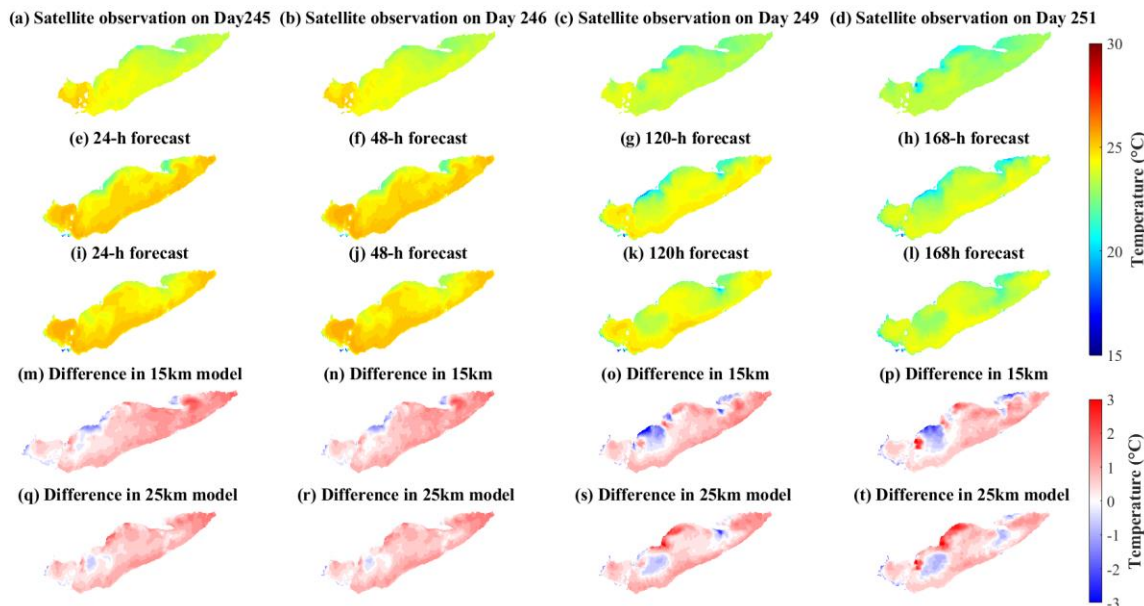
724



725

726 **Fig. D1 comparisons of (a-d) satellite observations, (e-h) 15 km model 240-h forecast, and (i-l) 25 km model**
727 **240-h forecast during summer. The models were hot-started on Day 215. The difference between observations**
728 **and models are shown in (m-t).**

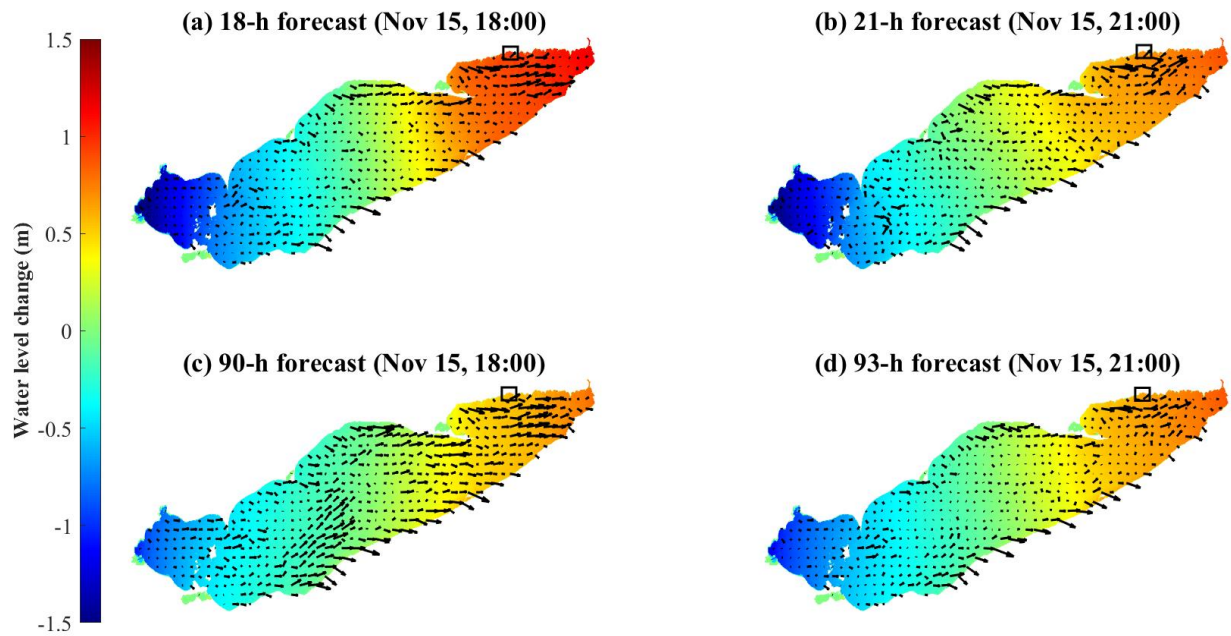
729



730

731 **Fig. D2 comparisons of (a-d) satellite observations, (e-h) 15 km model 240-h forecast, and (i-l) 25 km model**
732 **240-h forecast during late summer. The models were hot-started on Day 244. The difference between**
733 **observations and models are shown in (m-t).**

734 **Appendix E: Water level change during windstorm on Nov 15th, 2020**



735
736 **Fig. E1 Spatial distribution of water level change from forecasts hot-started on Nov 15th (a, b) and Nov 12th**
737 **(c, d). The water level at Nov 15th 00:00 is the reference level. The black arrows are depth-averaged mean**
738 **current fields. The black squares in the upper right corners of each map indicate the location of Port Dover**
739 **(Fig. 12d).**

740
741